

An Arbitrary Lagrangian-Eulerian Discontinuous Galerkin Scheme for Compressible Multi-Material Flows on Adaptive Quadrilateral Meshes

Xiaolong Zhao¹, Shicang Song¹, Xijun Yu², Shijun Zou^{3,*} and Fang Qing⁴

¹ School of Mathematics and Statistics, Zhengzhou University, Zhengzhou 450001, P.R. China.

² Laboratory of Computational Physics, Institute of Applied Physics and Computational Mathematics, Beijing 100088, P.R. China.

³ School of Mathematical Sciences, Capital Normal University, Beijing 100048, P.R. China.

⁴ School of Mathematics and Statistics, Hunan First Normal University, Changsha 410205, P.R. China.

Received 10 January 2023; Accepted (in revised version) 13 April 2023

Abstract. In this paper, a direct arbitrary Lagrangian-Eulerian (ALE) discontinuous Galerkin (DG) scheme is proposed for simulating compressible multi-material flows on the adaptive quadrilateral meshes. Our scheme couples a conservative equation related to the volume-fraction model with the Euler equations for describing the dynamics of the fluid mixture. The coupled system is discretized in the reference element and we use a kind of Taylor expansion basis functions to construct the interpolation polynomials of the variables. We show the property that the material derivatives of the basis functions in the DG discretization are equal to zero, with which the scheme is simplified. In addition, the mesh velocity in the ALE framework is obtained by using the adaptive mesh method from [H.Z. Tang and T. Tang, Adaptive mesh methods for one-and two-dimensional hyperbolic conservation laws, SIAM J. NUMER. ANAL.]. This adaptive mesh method can automatically concentrate the mesh nodes near the regions with large gradient values and greatly reduces the numerical dissipation near the material interfaces in the simulations. With the help of this adaptive mesh method, the resolution of the solution near the target regions can be greatly improved and the computational efficiency of the simulation is increased. Our scheme can be applied in the simulations for the gas and water media efficiently, and it is more concise compared to some other methods such as the indirect ALE methods. Several examples including the gas-water flow problem are presented to demonstrate the efficiency of our scheme,

*Corresponding author. Email addresses: xiaolongzhao109@zzu.edu.cn (X. Zhao), songshicang@zzu.edu.cn (S. Song), yuxj@iapcm.ac.cn (X. Yu), zoushijun@cnu.edu.cn (S. Zou), qingfang46@126.com (F. Qing)

and the results show that our scheme can capture the wave structures sharply with high robustness.

AMS subject classifications: 65M60, 35Q31, 76M10

Key words: Compressible multi-material flows, Arbitrary Lagrangian-Eulerian, Adaptive quadrilateral meshes, Discontinuous Galerkin scheme, Volume-fraction model.

1 Introduction

The hydrodynamics of multi-material flows such as gas and water is of great interest in Computational Fluid Dynamics (CFD) and exists in many problems such as the underwater explosion and the Inertial Confinement Fusion (ICF), etc. It has a wide application background in the fields of national economy and energy, etc. Its simulation has always been one of the difficult and frontier problems in the field of the fluid simulation. The simulation of compressible multi-material flows has the great theoretic significance and application value for understanding the physical phenomena in nuclear physics, biological engineering, and many other research fields. So, the research for the numerical simulations of compressible multi-material flows has obtained more and more attention from the scholars in recent years.

The multi-material fluid flows have some challenging problems in both theory and numerical simulations. The Eulerian method and the Lagrangian method are two kinds of classical methods used for dealing with multi-material flows. The Eulerian method [1–4] has strong robustness for solving the cases with large deformations, and the high-resolution schemes like essentially non-oscillatory (ENO) schemes, etc. [5, 6] based on the Eulerian method perform well when they are applied into the simulations of the single-material flow. However, when these algorithms are applied into the simulations of the multi-material cases, due to the numerical inaccuracies caused by the transport calculation, it is quite difficult for them to capture the precise physical interfaces. The Lagrangian method [7–14] has been studied by many scholars such as Després [7], Maire [8, 12], Rieben [10, 11] and Shashkov [13, 14], et al. This method can catch the material interfaces clearly in the simulations of multi-material flows. However, the large mesh distortions may lead to the interruptions of the computational codes or some errors in the simulations with large deformations, and these schemes need to introduce the mesh rezoning phase and the variables remapping phase for avoiding the large mesh distortions. For combining the advantages of this two kinds of methods above, Hirt et al. [15] has presented an arbitrary Lagrangian-Eulerian (ALE) method whose mesh nodes can move with the arbitrary velocity. The ALE method can flexibility simulate the flows with large deformations and moving regions. There are two kinds of ALE methods. The first one called indirect ALE method [16–18] consists of three steps: a Lagrangian step, a mesh rezoning step, and a variables remapping step. The second one called direct ALE method [19–21] consists of two steps: the step for obtaining the mesh velocity, the step

for discretizing the system which includes the mesh velocity. Without the need of considering the remapping step, the direct ALE method is concise and can be applied to construct the high-order schemes more easily than the ones with remapping step. There are quite a few papers which use the direct ALE formulation to handle compressible flows. For instance, Wang et al. [22] have developed a high-order accurate reconstructed discontinuous Galerkin (rDG) method for the two-dimensional hydrodynamic problems in the cell-centered updated Lagrangian formulation. This method is the Lagrangian limit of the unsplit rDG-ALE formulation which is obtained by assuming the equality of the mesh velocity to the fluid velocity only at cell boundaries. A number of benchmark tests are conducted to assess the accuracy, robustness, and non-oscillatory property of this developed rDG method [22]. Then, Wang et al. [23] have presented a high-order reconstructed discontinuous Galerkin method for compressible inviscid and viscous flows in arbitrary Lagrangian-Eulerian formulation on moving and deforming unstructured curved meshes. Some benchmark test cases involving the variable geometries are simulated to assess the accuracy and robustness of this rDG-ALE method [23] for moving and deforming boundary problems. Considering the features of the direct ALE method, a research about a direct ALE type scheme for multi-material flows will be present in this work.

Some difficulties such as the numerical oscillations may arise at material interfaces in the implementations of the conservative methods for multi-material flows. In recent decades, significant progress has been obtained in the development of the numerical schemes for simulating multi-material flows, one can see e.g. [24–28]. In [25], Abgrall and Karni have reviewed some numerical algorithms which had been proposed, and they have pointed the common key ideas that the algorithms possessed. Among these schemes, an extended system including the Euler equations has been studied in which additional equations were used to describe the evolutions of the fluid parameters such as the volume-fraction, the level set function or the ratio of specific heats of the fluid mixture. For maintaining the pressure equilibrium and eliminating the spurious oscillations near the regions involving the material interfaces, many scholars have studied various models (e.g: the volume-fraction model, the level-set model, etc), and they have proposed several schemes with an additional non-conservative equation for describing the fluid mixture, one can see e.g. [25]. In this work, we will construct a conservative scheme combining with an additional conservative equation for multi-material flows including the compressible ideal gases or water medium, and a volume-fraction model [29–31] which belongs to the diffusion interface models will be chosen to obtain the equation of state (EOS) of the fluid mixture.

One of the effective approaches for reducing the numerical errors of the simulations is combining the moving mesh methods with the schemes, so that the schemes can obtain the high-resolution numerical solutions with relatively few elements and less computational cost. In the past decades, many moving mesh methods have been studied by the scholars such as the variational approach presented of Winslow [32], the moving finite element method of Miller [33], and the moving mesh PDEs method of Cao et al. [34]. A

typical one of these methods is the R-type adaptive mesh moving method, and it is implemented by redistributing the mesh points to the interesting portions of the physical domain for resolving the large solution variations, without changing the topology of the mesh. The R-type adaptive methods are widely used in various schemes, which firstly aims at avoiding the serious distortion of mesh. Moreover, another important aim of this kind of methods is concentrating the mesh nodes with fixed topological structure on the regions with large gradient values of variables to improve the resolution of the specified regions. Tang et al. [35] developed a kind of R-type adaptive moving mesh algorithms based on the variational principle for the hyperbolic conservation laws, and the R-type adaptive algorithms effectively improved the resolution of the numerical solution. Then, Tang et al. [36] applied the adaptive mesh method [35] into the simulations of the two- and three-dimensional Hamilton-Jacobi equations, and the adaptive mesh increased the qualities of the solutions, similarly. Moreover, Tang et al. [37–39] also proposed a series of entropy stable adaptive moving mesh schemes for two- and three-dimensional special relativistic (magneto) hydrodynamics and (multi-component) compressible Euler equations with the stiffened equation of state respectively, and the excellent performance of these schemes was shown by several numerical examples. Li et al. [40] used the generalized Riemann problem (GRP) solver to develop an adaptive generalized Riemann problem (AGRP) scheme for one- and two- dimensional compressible flows with the adaptive moving quadrilateral meshes [35]. Ni et al. [41] developed a direct ALE type kinetic finite volume scheme with the numerical fluxes obtained by using the Bhatnagar-Gross-Krook (BGK) model on the adaptive quadrilateral mesh [35], and the mesh velocity given by the adaptive mesh method helped the presented scheme resolve the wave structures clearly. Although the R-type adaptive moving mesh methods have shown the effectiveness, their extensions and applications for the simulations of compressible multi-material flows is still relatively few and is worth studying. So, the authors consider that the researches of the simulations of compressible multi-material flows with the R-type adaptive moving mesh methods is quite meaningful.

The DG method is a numerical simulation method widely used for handling various models in many fields, e.g. compressible flows involving complex geometries and discontinuities. The solution of model is approximated with the help of base functions in each element by DG method, which leads to a direct piecewise high-order representation of solution. Boscheri et al. [42] proposed a high-order accurate nodal DG method for the solution of nonlinear hyperbolic systems of partial differential equations on unstructured polygonal Voronoi meshes. Liu et al. [43] developed a high-order DG method for solving the incompressible Navier-Stokes equations with variable density. Xia et al. [44] proposed a high-order accurate DG method for the compressible Euler equations under gravitational fields on unstructured meshes. Chen et al. [45] developed an adaptive modal DG finite element parallel method with unsplit multi-axial perfectly matched layer to simulate the seismic wave propagation. Coupling the features of the ALE scheme with the DG method, the ALE-DG method can deal with the discontinuities flexibly and efficiently in the simulations of compressible fluid flows. Considering the obvious advantages of

the ALE-DG method and the adaptive moving meshes for handling with the problems involving complex fluid flow, we mainly study a simple and high-efficiency ALE-DG scheme for compressible multi-material flows on the adaptive quadrangular meshes in this paper. In our scheme, the Euler equations couple with a conservative equation of the volume-fraction of the fluid are discretized by the DG method in the general element, and the conservative equation of the volume-fraction is used to describe the fluid composition for obtaining the equation of state (EOS) of the fluid mixture. Then the governing equations are transformed into the corresponding forms in the reference element with the help of the standard bilinear mapping, and they are discretized with the Taylor basis functions. There are quite a few papers in which the schemes define the basis functions on the reference element. For example, Liu et al. [46] have presented a high-order Lagrangian discontinuous Galerkin hydrodynamic method for compressible flows that is up to third-order accurate using the Taylor basis functions in the reference element. In addition, a specific property that the material derivatives of the Taylor basis functions are equal to zero when they are transformed into the corresponding forms in the general element is shown. With this property, our ALE-DG scheme does not need to consider the items involving the material derivatives of the basis functions which may not be evolved easily, and then the process of the discretization is greatly simplified. The velocity of mesh motion for our ALE scheme is obtained by the approach based on the variational principle [35]. This approach not only can make the new mesh maintain good quality but also can make the mesh nodes automatically converge near the regions involving large gradient values. Using this approach, our scheme have obtained the meshes and the solutions with good qualities. Finally, a Weighted Essentially Non-oscillatory (WENO) reconstruction on the quadrangular meshes is used to remove the spurious numerical oscillations near the discontinuities.

The innovation of this work is combining the ALE method, the DG method with the adaptive moving quadrilateral meshes to obtain a high-efficiency ALE-DG scheme for simulating multi-material flows. It is important to note that our scheme only applies to two-component flows involving the compressible ideal gases or water medium in two-dimensional geometry, and we will study the extension of this scheme for obtaining the wider scope of application in the future. In our work, the hydrodynamic Euler equations are coupled with a conservative equation associated with the volume-fraction for describing the fluid components. This coupling system can help our scheme simulate multi-material flows easily. This approach for describing the multi-material fluid is often used in the Eulerian methods and this work will apply it into the direct ALE-DG method with the adaptive quadrilateral meshes as a new attempt for the simulations of multi-material flows. The physical process of flows near the large deformation interface is complex, and material mixing and vorticity deposition often occur. In this event, the changes of the topology of the interfaces such as breakage and merger may occur, whether the clear material interfaces still exist has become a problem, so the pure Lagrangian description with clear-cut interfaces can no longer reflect the real physical process. Our ALE-DG method based on the volume-fraction model is simple, practical and robust. It

takes into account both the material components and the locations of the interfaces, and it is suitable for simulating the large deformation flow fields containing material mixing. Nevertheless, the disadvantage of the methods based on the diffusion interface models is that the numerical dissipation is large, and they are not suitable for the simulations which should obtain the interface positions accurately. In order to keep the compact thickness of material interfaces during computation, special numerical technologies such as the anti-diffusion technologies are needed to control the numerical dissipation at the material interfaces. In our scheme, because of the adaptive concentration of the mesh nodes near the discontinuities, to a certain extent the adaptive mesh moving method can help our scheme alleviate the problem of high dissipation near the material interfaces and capture the interfaces relatively clearly without other special numerical technologies.

Compared with the Lagrangian schemes, our scheme can simulate the wave structures clearly while ensuring the better quality of the meshes and can make the simulations run over longer time without the additional mesh repair algorithms. Compared with the indirect ALE schemes, without considering the remapping phase for the variables, our scheme is compact and it can avoid the influence of the remapping phase on the accuracy of the whole algorithm. Compared with the Eulerian schemes on the moving quadrilateral meshes [35, 36, 40], our scheme also need not consider the step of the variables interpolation from the old mesh to the new one. We have used several examples to demonstrate the good properties of our scheme, some of which are just as follows. In the radially symmetric underwater explosion problem, compared with the Eulerian methods, our scheme not only can precisely obtain the sharper shock waves with good-quality mesh but also consume less computational cost and fewer mesh elements. In the triple point problem, our scheme not only captures the vortexes clearly but also can run a long time meanwhile keeping the mesh good-quality. These examples have verified the good capabilities of simulating multi-material flows by our scheme. From what the authors have seen, this work is the first application of the direct ALE-DG method for simulating multi-material flows on the adaptive quadrilateral meshes. The authors consider that the results obtained by our scheme is competitive and our scheme has certain value in the field of the simulations of multi-material flows.

The outline of the rest of this paper is organized as follows. In Section 2, the governing equations are provided. In Section 3, the individual steps of simulating compressible multi-material flows by the ALE-DG scheme are shown. In Section 4, several examples are used to assess the good properties of our scheme. Finally, some concluding remarks for this work is shown in Section 5.

2 Governing equations

The Euler equations for inviscid compressible flows can be expressed as follows:

$$\begin{cases} \frac{\partial \rho}{\partial t} + \nabla \cdot (\rho \mathbf{V}) = 0, \\ \frac{\partial (\rho \mathbf{V})}{\partial t} + \nabla \cdot (\rho \mathbf{V} \otimes \mathbf{V}) + \nabla p = 0, \\ \frac{\partial (\rho E)}{\partial t} + \nabla \cdot (\rho E \mathbf{V}) + \nabla \cdot (p \mathbf{V}) = 0, \end{cases} \quad (2.1)$$

where ρ is the density, $\mathbf{V} = (u, v)$ is the velocity vector, p is the pressure, E denotes the specific total energy of the fluid, t is the time instant, and $\mathcal{E} = E - \frac{1}{2} \|\mathbf{V}\|^2$ denotes the specific internal energy. For the sake of clarity, we define $\mathbf{U} = (\rho, \rho \mathbf{V}, \rho E)$.

In the present work, our interest is centered on the perfect gases and the water media. The Euler equations are closed by an additional equation of state (EOS) for the perfect gases or the water medium which can be described uniformly as the form for the "stiffened" gas EOS:

$$p = (\gamma - 1)\rho \mathcal{E} - \gamma B, \quad (2.2)$$

where γ denotes the effective ratio of specific heats of fluid mixture, B is a prescribed pressure-like constant, and they depend on the fluid compositions of fluid flows. In many schemes, a new variable (we can define it as Φ) is always used to describe the fluid composition, and a non-conservative equation for Φ with the following form is chosen to obtain the EOS of the fluid mixture:

$$\frac{\partial \Phi}{\partial t} + \mathbf{V} \cdot (\nabla \Phi) = 0. \quad (2.3)$$

Eq. (2.3) should be solved specially because of the non-conservative form. In this paper, we combine Eq. (2.3) with the conservation law of mass to obtain a conservative form of Φ :

$$\frac{\partial (\rho \Phi)}{\partial t} + \nabla \cdot (\rho \Phi \mathbf{V}) = 0, \quad (2.4)$$

which is used for describing the dynamics of the fluid mixture.

Some choices of Φ which depend on the model assumptions have been studied in other literatures. For example, Φ can be set to the ratio of specific heats, the volume-fraction, or the level-set function, etc. In this work, the interface of two materials with different γ (or B) will be considered as a contact discontinuity of γ (or B), we will use the following volume-fraction model [29–31] with the volume-fraction Φ to describe the fluid compositions and obtain effective EOS of the fluid mixture.

To close the system, we will adopt the isobaric assumption in [30]. That is, the pressure for each fluid of the mixture is equal to each other in a mixed element. The EOS of the fluid mixture can be expressed by

$$p = (\bar{\gamma} - 1)\rho \mathcal{E} - \bar{\gamma} \bar{B}. \quad (2.5)$$

The average specific heat ratio $\bar{\gamma}$ and the average pressure-like constant \bar{B} of the fluid mixture are obtained by

$$\frac{1}{\bar{\gamma}-1} = \frac{\Phi_1}{\gamma_1-1} + \frac{\Phi_2}{\gamma_2-1}, \quad (2.6)$$

$$\bar{B} = \frac{\bar{\gamma}-1}{\bar{\gamma}} \left(\Phi_1 \frac{\gamma_1 B_1}{\gamma_1-1} + \Phi_2 \frac{\gamma_2 B_2}{\gamma_2-1} \right), \quad (2.7)$$

where $\Phi_1 = \Phi$ (or $\Phi_2 = (1-\Phi)$) denotes the volume-fraction of composition '1' (or composition '2'), γ_1 (or γ_2) denotes the specific heat ratio of composition '1' (or composition '2'), and B_1 (or B_2) denotes the pressure-like constant of composition '1' (or composition '2').

The conservative equation (2.4) can be coupled with the Euler equations just as follows:

$$\begin{cases} \frac{\partial \rho}{\partial t} + \nabla \cdot (\rho \mathbf{V}) = 0, \\ \frac{\partial(\rho \mathbf{V})}{\partial t} + \nabla \cdot (\rho \mathbf{V} \otimes \mathbf{V}) + \nabla p = 0, \\ \frac{\partial(\rho E)}{\partial t} + \nabla \cdot (\rho E \mathbf{V}) + \nabla \cdot (p \mathbf{V}) = 0, \\ \frac{\partial(\rho \Phi)}{\partial t} + \nabla \cdot (\rho \Phi \mathbf{V}) = 0. \end{cases} \quad (2.8)$$

For obtaining the EOS of fluid mixture and accomplishing the simulation of flow field, we design our algorithm as follows.

Step 1. Define the initial value of the volume-fraction Φ . We set the initial value $\Phi = (\Phi_1)_{t=0} = 1$ for the fluid composition '1' and $(\Phi_2)_{t=0} = 0$ for the fluid composition '2'.

Step 2. At a certain time step, we obtain $(\rho \Phi)$ and ρ of the fluid mixture by solving Eq. (2.8). Then, Φ is locally computed from the quotient $\Phi = \frac{(\rho \Phi)}{\rho}$, and Φ_1 and Φ_2 can be obtained simultaneously.

Step 3. With the isobaric assumption, we acquire the $\bar{\gamma}$ and \bar{B} of fluid mixture at this time step.

Step 4. With $\bar{\gamma}$, \bar{B} and the uniform EOS (2.5), we implement the numerical simulation at the next time step.

3 The process of simulating multi-material flows by the ALE-DG scheme

3.1 Some notations and the basis functions

The space discretization is accomplished by the DG method in this paper. The initial domain is set to Ω_0 , and we discretize the initial domain into a set of non-overlapping

quadrilaterals $\{(\Omega_0)_{ij}, i=1, \dots, M, j=1 \dots N\}$ with a total of $M \times N$ elements. Supposing Ω_t is the general region with coordinates (x, y) at time t which is filled by the inviscid fluid, we let $\{\mathcal{D}_{ij}, i=1, \dots, M, j=1 \dots N\}$ denote a collection of non-overlapping quadrilaterals whose reunion covers Ω_t and let \mathcal{D}_{ij} denote the element located at the j th row and i th column of the mesh structure. The vertices of \mathcal{D}_{ij} denoted by \mathcal{V}_{ijr} ($r=1, \dots, 4$) are indexed by counter clockwise, and we define the coordinates of \mathcal{V}_{ijr} as (x_{ijr}, y_{ijr}) . In addition, we let $\mathbf{V}^s = (u^s, v^s)$ be the mesh velocity vector of any point in Ω_t . As time progresses, the new partition $\{\mathcal{D}_{ij}, i=1, \dots, M, j=1, \dots, N\}$ will be obtained with the mesh velocity at the mesh node.

Then, we define the two-dimensional reference element as the bi-unit square $\mathcal{D}_0 = [-1, 1]^2$ with coordinates (X, Y) , where X and $Y \in [-1, 1]$. Using the bilinear finite element shape functions ψ_r ($r=1, \dots, 4$) as follows:

$$\begin{aligned} \psi_1(X, Y) &= \frac{1}{4}(1-X)(1-Y), & \psi_2(X, Y) &= \frac{1}{4}(1+X)(1-Y), \\ \psi_3(X, Y) &= \frac{1}{4}(1+X)(1+Y), & \psi_4(X, Y) &= \frac{1}{4}(1-X)(1+Y), \end{aligned}$$

each physical space element \mathcal{D}_{ij} ($i=1 \dots M, j=1 \dots N$) at time t can be related to the reference element by a map

$$\mathcal{A}_t: (X, Y) \in \mathcal{D}_0 \longrightarrow (x, y) \in \mathcal{D}_{ij}. \tag{3.1}$$

In more detail, the map can be expressed as

$$x = \sum_{r=1}^4 x_{ijr} \psi_r(X, Y), \quad y = \sum_{r=1}^4 y_{ijr} \psi_r(X, Y). \tag{3.2}$$

In Subsection 3.2, a DG scheme with a kind of linear Taylor basis functions defined in the reference element as follows:

$$\sigma_1 = 1, \quad \sigma_2 = X, \quad \sigma_3 = Y, \quad \sigma_4 = XY, \tag{3.3}$$

will be used to accomplish the space discretization. With the map \mathcal{A}_t , each Taylor basis function in the reference element \mathcal{D}_0 can be transformed into a corresponding function in element \mathcal{D}_{ij} :

$$\chi_r(x, y, t) = \sigma_r(X(x, y, t), Y(x, y, t)), \quad r=1, \dots, 4. \tag{3.4}$$

So, the functions $\chi_r(x, y, t)$ ($r=1, \dots, 4$) have a property that their material derivatives are equal to zero: $\frac{d\chi_r}{dt} = 0$. Analogously, with map \mathcal{A}_t , each bilinear finite element shape function ψ_r in the reference element \mathcal{D}_0 can also be transformed into a shape function in element \mathcal{D}_{ij} :

$$\phi_r(x, y, t) = \psi_r(X(x, y, t), Y(x, y, t)), \quad r=1, \dots, 4. \tag{3.5}$$

With the crucial property $\frac{d\chi_r}{dt} = 0$, we need not consider the items involving $\frac{d\chi_r}{dt}$ in the scheme, and then our scheme is simplified. This is one of the reasons why we choose this kind of basis functions for the space discretization, and one can refer to [47] for a more detailed proof of this property.

3.2 The spatial discretization

Firstly, the weak formulation of Eq. (2.8) will be introduced. For any test function $\varphi(x,y) \in L_2(\Omega_t)$, multiplying both sides of (2.8) by $\varphi(x,y)$ and integrating them on Ω_t , we can get the following form:

$$\begin{cases} \int_{\Omega_t} \frac{\partial \rho}{\partial t} \varphi d\Omega_t + \int_{\Omega_t} \nabla \cdot (\rho \mathbf{V}) \varphi d\Omega_t = 0, \\ \int_{\Omega_t} \frac{\partial(\rho \mathbf{V})}{\partial t} \varphi d\Omega_t + \int_{\Omega_t} (\nabla \cdot (\rho \mathbf{V} \otimes \mathbf{V}) + \nabla p) \varphi d\Omega_t = 0, \\ \int_{\Omega_t} \frac{\partial(\rho E)}{\partial t} \varphi d\Omega_t + \int_{\Omega_t} \nabla \cdot (\rho E \mathbf{V} + p \mathbf{V}) \varphi d\Omega_t = 0, \\ \int_{\Omega_t} \frac{\partial(\rho \Phi)}{\partial t} \varphi d\Omega_t + \int_{\Omega_t} \nabla \cdot (\rho \Phi \mathbf{V}) \varphi d\Omega_t = 0. \end{cases} \quad (3.6)$$

Secondly, we define the finite-element space as the following set of piecewise polynomials:

$$(\Omega_t)_h = \{ \varphi_h \in L_2(\Omega_t) : \varphi_h|_{\mathcal{D}_{ij}} \in P(\mathcal{D}_{ij}); 1 \leq i \leq M, 1 \leq j \leq N \},$$

where $P(\mathcal{D}_{ij})$ denotes a set of polynomials defined in the element \mathcal{D}_{ij} . Thirdly, we give the Reynolds transport theorem which will be used as follows. Let $v \in \Omega_t^{1,\infty}(0, T, H^1(\Omega_t))$, for all test functions $\varphi_h \in (\Omega_t)_h$, the Reynolds transport theorem can be expressed as the following form:

$$\frac{d}{dt} \int_{\mathcal{D}_{ij}} v \varphi_h d\mathcal{D}_{ij} = \int_{\mathcal{D}_{ij}} \frac{\partial(v \varphi_h)}{\partial t} d\mathcal{D}_{ij} + \int_{\partial \mathcal{D}_{ij}} v \varphi_h \mathbf{V}^g \cdot \mathbf{n} dS, \quad (3.7)$$

where $\partial \mathcal{D}_{ij}$ denotes the boundary of \mathcal{D}_{ij} , and $\mathbf{n} = (n_1, n_2)$ is the unit outward normal vector of $\partial \mathcal{D}_{ij}$. Then, the remaining process of the spatial discretization is implemented as follows.

For all test functions $\varphi_h \in (\Omega_t)_h$ and all elements \mathcal{D}_{ij} , we should find the approximate function $\mathbf{U}_h = (\rho_h, (\rho \mathbf{V})_h, (\rho E)_h, (\rho \Phi)_h) \in (\Omega_t)_h$ that satisfies

$$\begin{cases} \int_{\mathcal{D}_{ij}} \frac{\partial \rho_h}{\partial t} \varphi_h d\mathcal{D}_{ij} + \int_{\mathcal{D}_{ij}} \nabla \cdot (\rho \mathbf{V})_h \varphi_h d\mathcal{D}_{ij} = 0, \\ \int_{\mathcal{D}_{ij}} \frac{\partial(\rho \mathbf{V})_h}{\partial t} \varphi_h d\mathcal{D}_{ij} + \int_{\mathcal{D}_{ij}} (\nabla \cdot (\rho \mathbf{V} \otimes \mathbf{V})_h + \nabla p_h) \varphi_h d\mathcal{D}_{ij} = 0, \\ \int_{\mathcal{D}_{ij}} \frac{\partial(\rho E)_h}{\partial t} \varphi_h d\mathcal{D}_{ij} + \int_{\mathcal{D}_{ij}} \nabla \cdot ((\rho E \mathbf{V})_h + (p \mathbf{V})_h) \varphi_h d\mathcal{D}_{ij} = 0, \\ \int_{\mathcal{D}_{ij}} \frac{\partial(\rho \Phi)_h}{\partial t} \varphi_h d\mathcal{D}_{ij} + \int_{\mathcal{D}_{ij}} \nabla \cdot (\rho \Phi \mathbf{V})_h \varphi_h d\mathcal{D}_{ij} = 0. \end{cases} \quad (3.8)$$

Using the Reynolds transport theorem (3.7), we can obtain

$$\begin{cases} \frac{d}{dt} \int_{\mathcal{D}_{ij}} \rho_h \varphi_h d\mathcal{D}_{ij} + \int_{\mathcal{D}_{ij}} \nabla \cdot (\rho_h (\mathbf{V}_h - \mathbf{V}^s)) \varphi_h d\mathcal{D}_{ij} = \int_{\mathcal{D}_{ij}} \frac{d\varphi_h}{dt} \rho_h d\mathcal{D}_{ij}, \\ \frac{d}{dt} \int_{\mathcal{D}_{ij}} (\rho \mathbf{V})_h \varphi_h d\mathcal{D}_{ij} + \int_{\mathcal{D}_{ij}} (\nabla \cdot ((\rho \mathbf{V})_h \otimes (\mathbf{V}_h - \mathbf{V}^s)) + \nabla p_h) \varphi_h d\mathcal{D}_{ij} = \int_{\mathcal{D}_{ij}} \frac{d\varphi_h}{dt} (\rho \mathbf{V})_h d\mathcal{D}_{ij}, \\ \frac{d}{dt} \int_{\mathcal{D}_{ij}} (\rho E)_h \varphi_h d\mathcal{D}_{ij} + \int_{\mathcal{D}_{ij}} \nabla \cdot ((\rho E)_h (\mathbf{V}_h - \mathbf{V}^s) + (p \mathbf{V})_h) \varphi_h d\mathcal{D}_{ij} = \int_{\mathcal{D}_{ij}} \frac{d\varphi_h}{dt} (\rho E)_h d\mathcal{D}_{ij}, \\ \frac{d}{dt} \int_{\mathcal{D}_{ij}} (\rho \Phi)_h \varphi_h d\mathcal{D}_{ij} + \int_{\mathcal{D}_{ij}} \nabla \cdot ((\rho \Phi)_h (\mathbf{V}_h - \mathbf{V}^s)) \varphi_h d\mathcal{D}_{ij} = \int_{\mathcal{D}_{ij}} \frac{d\varphi_h}{dt} (\rho \Phi)_h d\mathcal{D}_{ij}. \end{cases} \quad (3.9)$$

For simplicity, we rewrite Eq. (3.9) as

$$\frac{d}{dt} \int_{\mathcal{D}_{ij}} \mathbf{U}_h \varphi_h d\mathcal{D}_{ij} + \int_{\mathcal{D}_{ij}} \nabla \cdot (F(\mathbf{U}_h), G(\mathbf{U}_h)) \varphi_h d\mathcal{D}_{ij} = \int_{\mathcal{D}_{ij}} \frac{d\varphi_h}{dt} \mathbf{U}_h d\mathcal{D}_{ij}, \quad (3.10)$$

where

$$F(\mathbf{U}_h) = \begin{pmatrix} F_1 \\ F_2 \\ F_3 \\ F_4 \\ F_5 \end{pmatrix} = \begin{pmatrix} \rho_h (u_h - u^s) \\ (\rho u)_h (u_h - u^s) + p_h \\ (\rho v)_h (u_h - u^s) \\ (\rho E)_h (u_h - u^s) + (p u)_h \\ (\rho \Phi)_h (u_h - u^s) \end{pmatrix},$$

$$G(\mathbf{U}_h) = \begin{pmatrix} G_1 \\ G_2 \\ G_3 \\ G_4 \\ G_5 \end{pmatrix} = \begin{pmatrix} (\rho)_h (v_h - v^s) \\ (\rho u)_h (v_h - v^s) \\ (\rho v)_h (v_h - v^s) + p_h \\ (\rho E)_h (v_h - v^s) + (p v)_h \\ (\rho \Phi)_h (v_h - v^s) \end{pmatrix}.$$

With the help of the divergence theorem, Eq. (3.10) can be equivalently expressed as:

$$\frac{d}{dt} \int_{\mathcal{D}_{ij}} \mathbf{U}_h \varphi_h d\mathcal{D}_{ij} = R_{ij}(\mathbf{U}_h) + \int_{\mathcal{D}_{ij}} \frac{d\varphi_h}{dt} \mathbf{U}_h d\mathcal{D}_{ij}, \quad (3.11)$$

where

$$R_{ij}(\mathbf{U}_h) = \int_{\mathcal{D}_{ij}} F(\mathbf{U}_h) \partial_x \varphi_h + G(\mathbf{U}_h) \partial_y \varphi_h d\mathcal{D}_{ij} - \int_{\partial \mathcal{D}_{ij}} (F(\mathbf{U}_h) n_1 + G(\mathbf{U}_h) n_2) \varphi_h dS.$$

For the convenience of the calculations, we will transform (3.11) in each element \mathcal{D}_{ij} into the corresponding form in the reference element \mathcal{D}_0 with the map \mathcal{A}_t above. As mentioned in Subsection 3.1, we will use the Taylor basis functions in the reference element: $\sigma_1 = 1, \sigma_2 = X, \sigma_3 = Y, \sigma_4 = XY$ to carry out the spatial discretization. Here, we will define $P(\mathcal{D}_{ij})$ in \mathcal{D}_{ij} . Firstly, we define a function space in the reference element \mathcal{D}_0 as: $P(\mathcal{D}_0) =$

span $\{\sigma_1, \sigma_2, \sigma_3, \sigma_4\}$. Then, $P(\mathcal{D}_{ij})$ can be defined as a set of the transformed forms of the functions in $P(\mathcal{D}_0)$ with the map \mathcal{A}_t . Since all the test functions can make Eq. (3.11) hold, we choose $\chi_m (m = 1, \dots, 4)$ as the test function φ_h . With the property that the material derivatives of the basis functions χ_m are equal to zero, we can have $\frac{d\varphi_h}{dt} = \frac{d\chi_m}{dt} = 0$ in (3.11), and then the second item on the right-hand side of Eq. (3.11) becomes zero. For the sake of brevity, the interpolation polynomials in the finite element approximations and the test functions in the reference element are also denoted by \mathbf{U}_h and φ_h , respectively. Assuming U_h is any component of \mathbf{U}_h , we use the Taylor basis functions in \mathcal{D}_0 to rewrite U_h and φ_h as follows.

$$U_h(X, Y) = \sum_{r=1}^4 U_{ijr} \sigma_r, \quad \varphi_h(X, Y) = \sum_{r=1}^4 \varphi_{ijr} \sigma_r, \quad (X, Y) \in \mathcal{D}_0. \tag{3.12}$$

Duo to $\varphi_h(x, y) = \chi_m(x, y) (m = 1, \dots, 4)$ in the general element \mathcal{D}_{ij} , we have $\varphi_h(X, Y) = \sigma_m(X, Y) (m = 1, \dots, 4)$ in the reference element \mathcal{D}_0 respectively, and this is equivalent to setting $\varphi_{ijr} = 1$ for $r = m$ and $\varphi_{ijr} = 0$ for other case in (3.12). In addition, it can be verified that

$$\begin{pmatrix} \frac{\partial X}{\partial x} & \frac{\partial X}{\partial y} \\ \frac{\partial Y}{\partial x} & \frac{\partial Y}{\partial y} \end{pmatrix} = \begin{pmatrix} \frac{\partial x}{\partial X} & \frac{\partial x}{\partial Y} \\ \frac{\partial y}{\partial X} & \frac{\partial y}{\partial Y} \end{pmatrix}^{-1} = \frac{1}{J} \begin{pmatrix} \frac{\partial y}{\partial Y} & -\frac{\partial x}{\partial Y} \\ -\frac{\partial y}{\partial X} & \frac{\partial x}{\partial X} \end{pmatrix}, \tag{3.13}$$

where J is the determinant of Jacobian matrix:

$$J = \begin{vmatrix} \frac{\partial x}{\partial X} & \frac{\partial x}{\partial Y} \\ \frac{\partial y}{\partial X} & \frac{\partial y}{\partial Y} \end{vmatrix}. \tag{3.14}$$

With (3.13), for $\partial_x \varphi_h$ and $\partial_y \varphi_h$ in (3.11), we can have

$$\begin{cases} \partial_x \varphi_h = \frac{\partial \sigma_m}{\partial X} \frac{\partial X}{\partial x} + \frac{\partial \sigma_m}{\partial Y} \frac{\partial Y}{\partial x} = \frac{1}{J} \left(\frac{\partial \sigma_m}{\partial X} \frac{\partial y}{\partial Y} - \frac{\partial \sigma_m}{\partial Y} \frac{\partial y}{\partial X} \right) = \partial_x \sigma_m, \\ \partial_y \varphi_h = \frac{\partial \sigma_m}{\partial X} \frac{\partial X}{\partial y} + \frac{\partial \sigma_m}{\partial Y} \frac{\partial Y}{\partial y} = \frac{1}{J} \left(-\frac{\partial \sigma_m}{\partial X} \frac{\partial x}{\partial Y} + \frac{\partial \sigma_m}{\partial Y} \frac{\partial x}{\partial X} \right) = \partial_y \sigma_m. \end{cases} \tag{3.15}$$

Applying (3.12) and (3.15) into Eq. (3.11) and using $\frac{d\varphi_h(x,y)}{dt} = 0$, (3.11) can evolve into the following form:

$$\begin{aligned} \frac{d}{dt} \sum_{r=1}^4 \int_{\mathcal{D}_0} U_{ijr} \sigma_r \sigma_m J_{ij} d\mathcal{D}_0 &= R_{ij}(\mathbf{U}_h), \\ R_{ij}(\mathbf{U}_h) &= \int_{\mathcal{D}_0} (F(\mathbf{U}_h) \partial_x \sigma_m + G(\mathbf{U}_h) \partial_y \sigma_m) J_{ij} d\mathcal{D}_0 - \sum_{l=1}^4 \int_{\Gamma_l} (\widehat{F(\mathbf{U}_h)}, \widehat{G(\mathbf{U}_h)}) \cdot \mathbf{n} \sigma_m \frac{|L_l|}{2} d\Gamma_l, \end{aligned} \tag{3.16}$$

where J_{ij} is the determinant of the Jacobian matrix of the transformation of coordinates related to \mathcal{D}_0 and \mathcal{D}_{ij} , $|L_l|$ denotes the length of the element edge $L_l (l = 1, \dots, 4)$ that makes up the boundary of \mathcal{D}_{ij} . $(\widehat{F(\mathbf{U}_h)}, \widehat{G(\mathbf{U}_h)}) \cdot \mathbf{n}$ actually is the numerical flux at the element

edge L_l ($l = 1, \dots, 4$), and we transform it into the equivalent form at the element edge Γ_l that makes up the boundary of \mathcal{D}_0 . In this work, we choose the L-F (Lax-Friedrichs) flux as the replacement of the numerical flux.

Finally, we set

$$\begin{aligned} \mathbf{M}_{ij} &= \int_{\mathcal{D}_0} \sigma_r \sigma_m J_{ij} d\mathcal{D}_0, \quad (r = 1, \dots, 4; m = 1, \dots, 4), \\ (\widehat{\mathbf{U}}_h)_{ij1} &= [\rho_{ij1}, \rho_{ij2}, \rho_{ij3}, \rho_{ij4}]^T, \\ (\widehat{\mathbf{U}}_h)_{ij2} &= [(\rho u)_{ij1}, (\rho u)_{ij2}, (\rho u)_{ij3}, (\rho u)_{ij4}]^T, \\ (\widehat{\mathbf{U}}_h)_{ij3} &= [(\rho v)_{ij1}, (\rho v)_{ij2}, (\rho v)_{ij3}, (\rho v)_{ij4}]^T, \\ (\widehat{\mathbf{U}}_h)_{ij4} &= [(\rho E)_{ij1}, (\rho E)_{ij2}, (\rho E)_{ij3}, (\rho E)_{ij4}]^T, \\ (\widehat{\mathbf{U}}_h)_{ij5} &= [(\rho \Phi)_{ij1}, (\rho \Phi)_{ij2}, (\rho \Phi)_{ij3}, (\rho \Phi)_{ij4}]^T. \end{aligned} \quad (3.17)$$

Eq. (3.16) will evolve into

$$\frac{d}{dt} \mathbf{M}_{ij} \cdot (\widehat{\mathbf{U}}_h)_{ij} = R_{ij}(\mathbf{U}_h), \quad (3.18)$$

where $R_{ij}(\mathbf{U}_h)$ is the spatial discrete operator, and

$$(\widehat{\mathbf{U}}_h)_{ij} = [(\widehat{\mathbf{U}}_h)_{ij1}, (\widehat{\mathbf{U}}_h)_{ij2}, (\widehat{\mathbf{U}}_h)_{ij3}, (\widehat{\mathbf{U}}_h)_{ij4}, (\widehat{\mathbf{U}}_h)_{ij5}].$$

3.3 The geometric conservation law

In the simulations of fluid flow with the moving meshes, it is important to ensure that the scheme satisfies the geometric conservation law (GCL). That is to say, the numerical scheme with an initial uniform flow should preserve exactly a constant solution. The necessity of GCL for the numerical stability has been discussed by many scholars. Farhat et al. [48] showed that satisfying the corresponding discrete GCL (DGCL) is a necessary and sufficient condition for a numerical scheme to preserve the nonlinear stability in the sense of the discrete maximum principle of its fixed grid counterpart. Farhat et al. [48] also highlighted the impact of this theoretical result on the practical applications of computational fluid dynamics. Wang et al. [23] used a space-time type integration to obtain the discretized equations of rDG scheme in ALE formulation and then modified the grid velocity terms on the right-hand side of the discretized equations at Gauss quadrature points to make the high-order ALE rDG scheme preserve the GCL.

It's worth noting that our scheme is able to preserve the GCL in the semi-discrete form, but it does not guarantee the DGCL at present. In the future, we will continue to study the DGCL of our scheme. Here, we will show that our scheme is able to preserve the GCL in the semi-discrete form. In other words, our semi-discrete scheme (3.10) can preserve the uniform flow.

Let us consider the Eq. (2.8) with an initial constant value $\mathbf{U}_{t=0} = \mathbf{U}_0 = (\rho_0, (\rho \mathbf{V})_0, (\rho E)_0, (\rho \Phi)_0)$ in Ω_0 . So, the numerical solution of our scheme should be

preserved as \mathbf{U}_0 . The divergence of the flux functions which can be expressed as $\nabla \cdot (F(\mathbf{U}_0), G(\mathbf{U}_0))$ will become $(-\nabla \cdot \mathbf{V}^g)\mathbf{U}_0$ because of the constant value \mathbf{U}_0 , and the semi-discrete scheme (3.10) can be rewritten as

$$\frac{d}{dt} \int_{\mathcal{D}_{ij}} \varphi_h \mathbf{U}_0 d\mathcal{D}_{ij} - \int_{\mathcal{D}_{ij}} (\nabla \cdot \mathbf{V}^g) \varphi_h \mathbf{U}_0 d\mathcal{D}_{ij} = \int_{\mathcal{D}_{ij}} \frac{d\varphi_h}{dt} \mathbf{U}_0 d\mathcal{D}_{ij}. \quad (3.19)$$

Then, with the divergence theorem, we can have

$$\frac{d}{dt} \int_{\mathcal{D}_{ij}} \varphi_h \mathbf{U}_0 d\mathcal{D}_{ij} = \int_{\mathcal{D}_{ij}} \frac{\partial(\mathbf{U}_0 \varphi_h)}{\partial t} d\mathcal{D}_{ij} + \int_{\partial\mathcal{D}_{ij}} \mathbf{U}_0 \varphi_h \mathbf{V}^g \cdot \mathbf{n} dS, \quad (3.20)$$

which is the expression of the GCL form for the semi-discrete scheme (3.10). Finally, we can eliminate the constant value \mathbf{U}_0 and obtain

$$\frac{d}{dt} \int_{\mathcal{D}_{ij}} \varphi_h d\mathcal{D}_{ij} = \int_{\mathcal{D}_{ij}} \frac{\partial \varphi_h}{\partial t} d\mathcal{D}_{ij} + \int_{\partial\mathcal{D}_{ij}} \varphi_h \mathbf{V}^g \cdot \mathbf{n} dS. \quad (3.21)$$

It can be seen that (3.21) is exactly a expression of the transport equation (3.7) with $\nu = 1$. Thus, the semi-discrete scheme (3.10) preserves the constant solution and satisfies the GCL naturally.

3.4 The mesh velocity

For obtaining the appropriate meshes, we will study two factors to choose the approach of determining the mesh velocity \mathbf{V}^g . Firstly, the new meshes with good-quality should be smooth. Secondly, the new meshes should be automatically redistributed and concentrated at the regions involving large gradient values of some variables. The approach of the adaptive mesh movement in [35] based on the variational principle can satisfy these two factors, so we will choose this approach to obtain the mesh velocity.

3.4.1 The approach of mesh motion based on the variational principle

Firstly, we define the computational domain which has quasi-uniform mesh partition as W_l with the orthometric coordinates $\xi = (\xi, \eta)$, and we define the physical domain as W_p with coordinates $x = (x, y)$. A one-to-one coordinate transformation from the computational domain W_l to the physical domain W_p is denoted by

$$\mathbf{x} = \mathbf{x}(\xi), \quad \xi \in W_l. \quad (3.22)$$

In the variational approach, supposing W_p is a convex region, the transformation can be provided approximately by the minimizer of a functional with the following form:

$$\tilde{E}(\mathbf{x}) = \frac{1}{2} \sum_{k=1}^2 \int_{W_l} (\tilde{\nabla} \mathbf{x})^T G_k \tilde{\nabla} \mathbf{x} d\xi, \quad (3.23)$$

where $\tilde{\nabla} = (\partial_{\xi}, \partial_{\eta})$, and G_k ($k=1,2$) is given symmetric positive definite matrix named monitor function.

The monitor function is adaptive and depends on the variables (or their derivatives) of the underlying governing equations. One of the simple choices of the monitor functions is $G_k = \omega I$ ($k=1,2$), where I is an identity matrix and ω is positive piecewise constant. In this paper, the monitor function $\omega_{i,j}$ of element \mathcal{D}_{ij} is:

$$\omega_{i,j} = \sqrt{1 + \alpha_1 |\kappa_{i,j}|^2 + \alpha_2 |\tilde{\nabla} \kappa_{i,j}|^2}, \quad (3.24)$$

where α_1 and α_2 are some positive constants given in each example for controlling the movement of mesh, and κ can denote ρ , u, v , or p , etc. According to our experience, the reasonable selection range of these artificial coefficients α_1 or α_2 can be set to $[0,1]$ in general and the suitable coefficients should be obtained by debugging the codes of the simulations according to the specific examples.

Numerically, for obtaining the coordinate transformation (3.22), we can solve the equations:

$$\tilde{\nabla} \cdot (\omega \tilde{\nabla} \mathbf{x}) = 0. \quad (3.25)$$

Eq. (3.25) are the final target equations for the new mesh and they can be solved by a finite difference method. Then, we will use an iteration method to complete the discretization:

$$\mathbf{x}_{i,j}^{[v+1]} = \frac{\omega_1^{[v]} \mathbf{x}_{i+1,j}^{[v]} + \omega_2^{[v]} \mathbf{x}_{i-1,j}^{[v]} + \omega_3^{[v]} \mathbf{x}_{i,j+1}^{[v]} + \omega_4^{[v]} \mathbf{x}_{i,j-1}^{[v]}}{\omega_1^{[v]} + \omega_2^{[v]} + \omega_3^{[v]} + \omega_4^{[v]}}, \quad (3.26)$$

where $\mathbf{x}_{i,j}$ denote the coordinates of the mesh node located at the cross point of the j th horizontal grid line and the i th vertical grid line in the mesh structure ($i=1, \dots, (M+1); j=1, \dots, (N+1)$),

$$\begin{aligned} \omega_1^{[v]} &= \frac{1}{2}(\omega_{i+\frac{1}{2},j+\frac{1}{2}}^{[v]} + \omega_{i+\frac{1}{2},j-\frac{1}{2}}^{[v]}), & \omega_2^{[v]} &= \frac{1}{2}(\omega_{i-\frac{1}{2},j+\frac{1}{2}}^{[v]} + \omega_{i-\frac{1}{2},j-\frac{1}{2}}^{[v]}), \\ \omega_3^{[v]} &= \frac{1}{2}(\omega_{i+\frac{1}{2},j+\frac{1}{2}}^{[v]} + \omega_{i-\frac{1}{2},j+\frac{1}{2}}^{[v]}), & \omega_4^{[v]} &= \frac{1}{2}(\omega_{i+\frac{1}{2},j-\frac{1}{2}}^{[v]} + \omega_{i-\frac{1}{2},j-\frac{1}{2}}^{[v]}), \end{aligned}$$

v denotes the iterations, and

$$\omega_{i\pm\frac{1}{2},j\pm\frac{1}{2}} = \frac{1}{2}(\omega_{i\pm 1,j\pm 1} + \omega_{i,j}).$$

The iteration determines the locations of the new mesh nodes, and it is continued until there is no detectable change in the new mesh from one iteration to the next. Typically, the mesh movement for each time step requires 3 to 5 times iterations. For keeping the simulations steady and uniform, we choose 5 times iterations at each time step in this work.

Finally, the mesh velocity $(\mathbf{V}_{i,j}^g)^n$ of the mesh node with coordinates $\mathbf{x}_{i,j}$ at the n th time step $t = t_n$ can be obtained as follows:

$$(\mathbf{V}_{i,j}^g)^n = \frac{\mathbf{x}_{i,j}^{n+1} - \mathbf{x}_{i,j}^n}{(\Delta t)^n}, \quad (3.27)$$

where Δt is the time steplength and the symbols of the variables with superscript n (or $(n+1)$) denote the values of the corresponding variables at the n (or $(n+1)$)th time step. The time steplength at the n th time step is set to

$$(\Delta t)^n = \lambda \cdot \min_{i=1,\dots,M; j=1,\dots,N} \{(\Delta l_{ij}/\mathcal{C}_{ij})^n\}, \quad \mathcal{C}_{ij} = (|u_{ij} - u_{ij}^g| + c_{ij}) + (|v_{ij} - v_{ij}^g| + c_{ij}), \quad (3.28)$$

where Δl_{ij} denotes the length of the shortest edge in \mathcal{D}_{ij} , c_{ij} is the sound speed at the barycenter of \mathcal{D}_{ij} , and the values of other variables needed for obtaining $(\Delta t)^n$ are also set to the corresponding values at the barycenter of \mathcal{D}_{ij} . For keeping the scheme stable, the Courant number λ of the scheme should satisfy this condition: $\lambda \leq \frac{1}{3}$ which is detailed in [49, 50] and we will simulate the examples with $\lambda = 0.27$ in Section 4.

3.4.2 The technology of spatial smoothing

In the simulations, adding the temporal smoothing or the spatial smoothing on the monitor value ω to make the mesh smoother is useful. Using the smoothing technology can avoid producing very singular mesh and large approximation errors near the regions with large gradient values of some variables. In this work, we will apply the following technology into the smoothing of the monitor:

$$\begin{aligned} \omega_{i+\frac{1}{2}, j+\frac{1}{2}} \leftarrow & \frac{1}{4} \omega_{i+\frac{1}{2}, j+\frac{1}{2}} + \frac{1}{8} (\omega_{i-\frac{1}{2}, j+\frac{1}{2}} + \omega_{i+\frac{3}{2}, j+\frac{1}{2}} + \omega_{i+\frac{1}{2}, j-\frac{1}{2}} + \omega_{i+\frac{1}{2}, j+\frac{3}{2}}) \\ & + \frac{1}{16} (\omega_{i+\frac{3}{2}, j+\frac{3}{2}} + \omega_{i-\frac{1}{2}, j+\frac{3}{2}} + \omega_{i+\frac{3}{2}, j-\frac{1}{2}} + \omega_{i-\frac{1}{2}, j-\frac{1}{2}}). \end{aligned} \quad (3.29)$$

Then, we can obtain the new monitor value. Applying this smoothing technology 2 or 3 times, the approach of mesh movement can improve the mesh smoothness clearly.

3.5 The slope limiter and the time discretization

3.5.1 Time discretization

The semi-discrete system (3.18) can be integrated in time with the explicit methods directly. In this work, we will use the explicit second-order Total Variation Diminishing (TVD) Runge-Kutta (RK) scheme [49, 50] to accomplish the time discretization of Eq. (3.18). Besides the semi-discrete system, the mesh and the mass matrix of each element should be also updated at each RK stage because of the mesh movement. The readers can refer to [49, 50] for more details of the time-marching algorithm.

3.5.2 The slope limiter based on the WENO reconstruction

When the flows involving strong discontinuities are simulated by the DG scheme described above, the non-physical oscillations will be produced. So we will choose a WENO reconstruction as a non-linear slope limiter to control the oscillations in this work. For controlling the oscillations perfectly, we will implement this reconstruction after the update of each sub-stage of the time-marching algorithm.

Before implementing the reconstruction, firstly we let (x_e, y_e) denote the coordinates of the centroid of an arbitrary element e , and we define the symbol Δx or Δy as $\Delta x = x - x_e$ or $\Delta y = y - y_e$. Then, we compute the element average values of the variables. For instance, we focus on element e and an arbitrary variable denoted by w which can represent any component of $(\rho, \rho u, \rho v, \rho E, \rho \Phi)$. By solving Eq. (3.18), the Taylor expansion of w on the element e can be obtained. Next, we can get the element average value of variable w with the Gauss integration algorithm:

$$\bar{w}_e = \frac{1}{|e|} \int_e w dx dy, \quad (3.30)$$

where $|e|$ denotes the area of element e .

For our DG scheme, we will reconstruct a polynomial \hat{w} for the variable w on element e : $\hat{w} = \bar{w}_e + \tilde{w}_x \Delta x + \tilde{w}_y \Delta y$, where \bar{w}_e is the element average value of w on element e . It can be seen that the polynomial \hat{w} remains the element average value of w on the element e . There are still two undefined coefficients \tilde{w}_x and \tilde{w}_y in \hat{w} . We will evaluate this two coefficients with the WENO reconstruction algorithm for the DG scheme in [51], and one can see [51] for more details of the reconstruction. For clarity, we show the positional relationship of e and its eight related Neumann neighborhood elements denoted by a, b, \dots, g, i in Fig. 1.

After the process above is finished, we apply this new reconstruction to modify the coefficients of the Taylor expansion of variable w on the reference element. A L_2 projection procedure will be used for obtaining the revised coefficients of the Taylor expansion of w with the reconstructed polynomial \hat{w} of w on the general element e , and we still refer

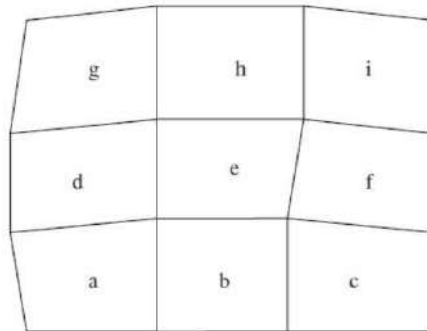


Figure 1: Element e and its eight nearest neighborhoods.

the reader to [51] for more details. Under the premise of remaining the average value of w on the element e , the revised Taylor expansion of w on the reference element retains the second-order accuracy in the smooth regions and can make the solutions oscillation-free near the discontinuities.

4 Numerical examples

In this section, we will simulate several examples to demonstrate the accuracy and the good performance of our scheme. If there is no special explanation, all the boundary conditions will be set to the wall boundary conditions, and the κ in the method of the adaptive mesh movement will be set to the density ρ . All the examples are simulated by the codes of our scheme on a PC with a CPU: Inter Core i7-8700(3.2GHz).

4.1 The accuracy test: Taylor-Green vortex problem

The first example is a vortical flow problem with an analytical solution [52]. It is actually a single-material case, and we only need to consider the Euler equations (2.1) in this simulation. The initial condition of this case is set to

$$\begin{aligned}\rho_0 &= 1, & p_0 &= \frac{1}{4}[\sin(2\pi x) + \cos(2\pi y)] + 1, \\ u_0 &= \sin(\pi x)\cos(\pi y), & v_0 &= -\cos(\pi x)\sin(\pi y),\end{aligned}$$

in the domain $(x, y) \in [0, 1] \times [0, 1]$. According to the characteristic of this example, the mesh vertex velocity is set to the adaptive velocity obtained by the adaptive mesh method using a special monitor function $\omega_{i,j}$ in element \mathcal{D}_{ij} : $\omega_{i,j} = \sqrt{1 + 200|p_{i,j} - \bar{p}|^2}$ in which \bar{p} denotes the average value of maximum pressure and minimum pressure at the barycenters of all elements in the whole domain. In addition, an approximate fluid velocity obtained by the approach in [53] are also used for testing this example. In the simulation of the compressible inviscid flow, an energy source term is used to make the solution be in the steady state,

$$S_E = \frac{\pi}{4(\gamma - 1)} [\cos(3\pi x)\cos(\pi y) - \cos(3\pi y)\cos(\pi x)].$$

The meshes and the pressure distributions of this case with 80×80 elements at $t = 0.75$ are shown in Fig. 2. The L^1 , L^2 , L^∞ errors and the corresponding convergence orders of our scheme for density ρ at $t = 0.75$ are shown in Table 1 and Table 2, respectively. It can be seen that our scheme achieves the second-order accuracy, and we obtain the satisfactory result containing the good-quality meshes and the appropriate pressure distributions on the moving quadrilateral meshes.

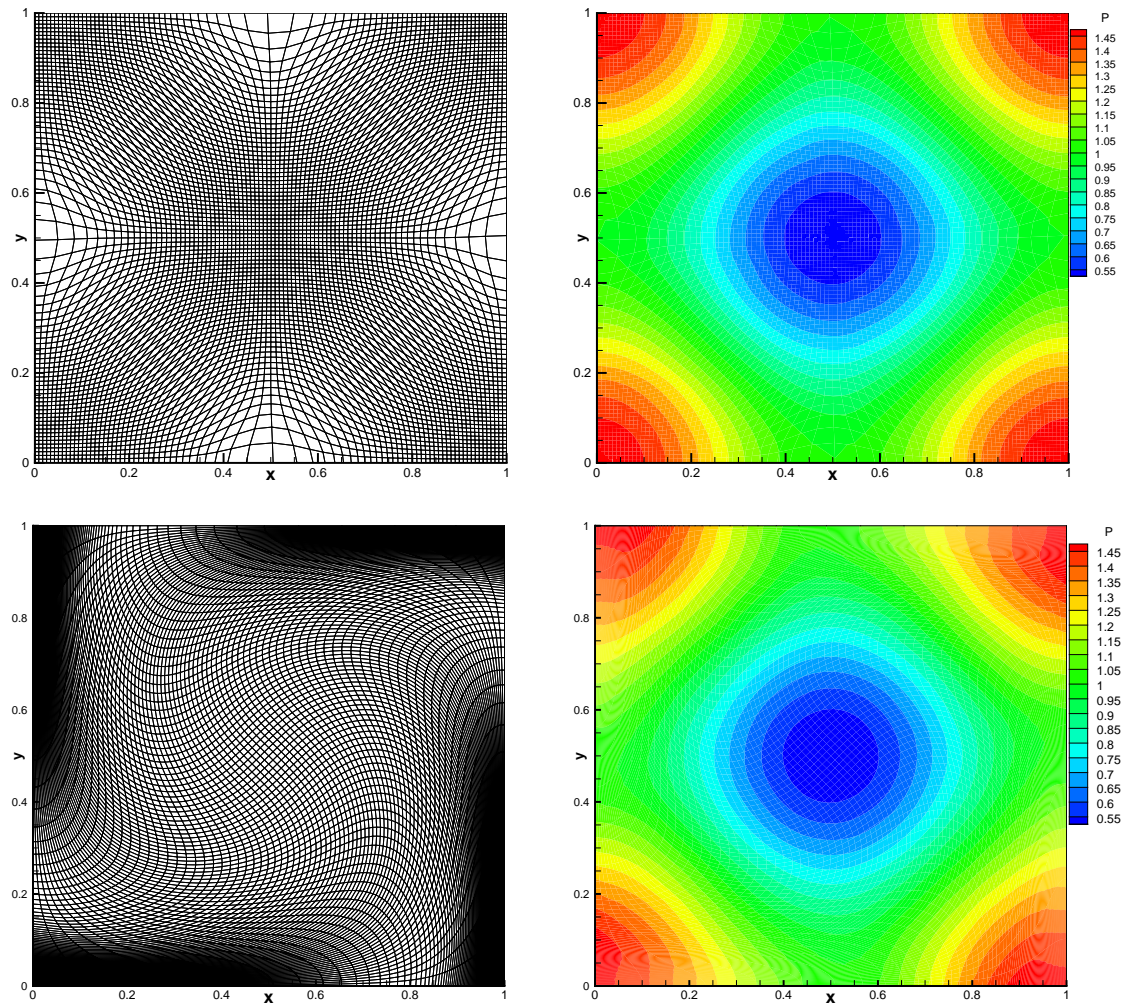


Figure 2: The results of the Taylor-Green vortex problem at $t=0.75$ for 80×80 elements. Left: the mesh; right: the pressure; top: the result obtained with the adaptive mesh method; bottom: the result obtained with the approximate fluid velocity in [53].

Table 1: The errors of density for Taylor-Green vortex problem obtained with the adaptive mesh method.

Elements	L^1 error	order	L^2 error	order	L^∞ error	order
10×10	2.2273E-002	-	3.4680E-002	-	1.1589E-001	-
20×20	8.3157E-003	1.4214	1.2145E-002	1.5137	5.7678E-002	1.0067
40×40	2.2976E-003	1.8557	3.9872E-003	1.6069	2.0232E-002	1.5114
80×80	5.9081E-004	1.9594	1.0172E-003	1.9708	6.6917E-003	1.5962
160×160	1.3947E-004	2.0827	2.5569E-004	1.9921	1.7469E-003	1.9376

Table 2: The errors of density for Taylor-Green vortex problem obtained with the approximate fluid velocity.

Elements	L^1 error	order	L^2 error	order	L^∞ error	order
10×10	2.5246E-002	-	3.7267E-002	-	1.4852E-001	-
20×20	8.8949E-003	1.5050	1.5221E-002	1.2918	6.7247E-002	1.1431
40×40	2.4377E-003	1.8675	4.4757E-003	1.7659	2.2815E-002	1.5595
80×80	6.3564E-004	1.9392	1.1693E-003	1.9365	7.2820E-003	1.6476
160×160	1.5835E-004	2.0051	2.9160E-004	2.0036	1.9310E-003	1.9150

4.2 The two-phase gas-liquid Riemann problem

The second example describes a two-phase gas-liquid Riemann problem. In this example, there is the gas phase with the initial data $(\rho, u, p, \gamma, B, \Phi)_L = (1.241, 0, 2.753, 1.4, 0, 1)$ on the left region: $x \in [0, 0.5)$, and there is the liquid phase with the initial data $(\rho, u, p, \gamma, B, \Phi)_R = (0.991, 0, 3.059 \times 10^{-4}, 5.5, 1.505, 0)$ on the right: $x \in [0.5, 1.0]$. In our work, we will run the simulation of this one-dimensional problem on a two-dimensional region $[0, 1.0] \times [0, 0.1]$ with the computational meshes consisting of 100×10 cells and 200×10 cells, respectively. The final time of this simulation is $t = 0.1$, and the artificial parameters of the adaptive mesh motion are set to $\alpha_1 = 0$ and $\alpha_2 = 0.6$. For obtaining the reference solution, we use the front-tracking algorithm for the radial symmetry (with 1000 computing elements) to solve the one-dimensional multicomponent model with appropriate source terms, whose derivation can be found in [54].

Fig. 3 shows our result at $t = 0.1$. As illustrated, we can see the good behavior of the computed wave structures. In addition, as the number of the mesh cells increases in the x -direction (from 100 cells to 200 cells), the contact discontinuity and the shock wave approximate the reference solution better. So, our scheme can capture the waves precisely and sharply, and this case shows the ability of our scheme in the simulations of multi-material flows.

4.3 The Dukowicz refraction problem

The Dukowicz refraction problem involves a shock wave interacting with the interface which has been tested by many scholars with different schemes, see for example, [55, 56]. In this refraction problem, a vortex sheet is generated by the interaction of a shock wave with an inclined material interface. The initial domain with the mesh partition is shown in Fig. 4. The left region has 37×30 mesh elements with a vertical left boundary and a right boundary aligned at 30° to the horizontal direction, and the right region has 53×30 mesh elements with uniformly slanted at 30° to the horizontal direction. In [55, 56], the computational domain consists of two adjacent regions whose gases have different densities but equal pressure, and the two regions are all filled up with the single ideal gas which have $\gamma = 1.4$. Here, we simulate this problem with two materials of different γ (1.4 and 1.67) and then makes it be a two-material case which contains an 'material

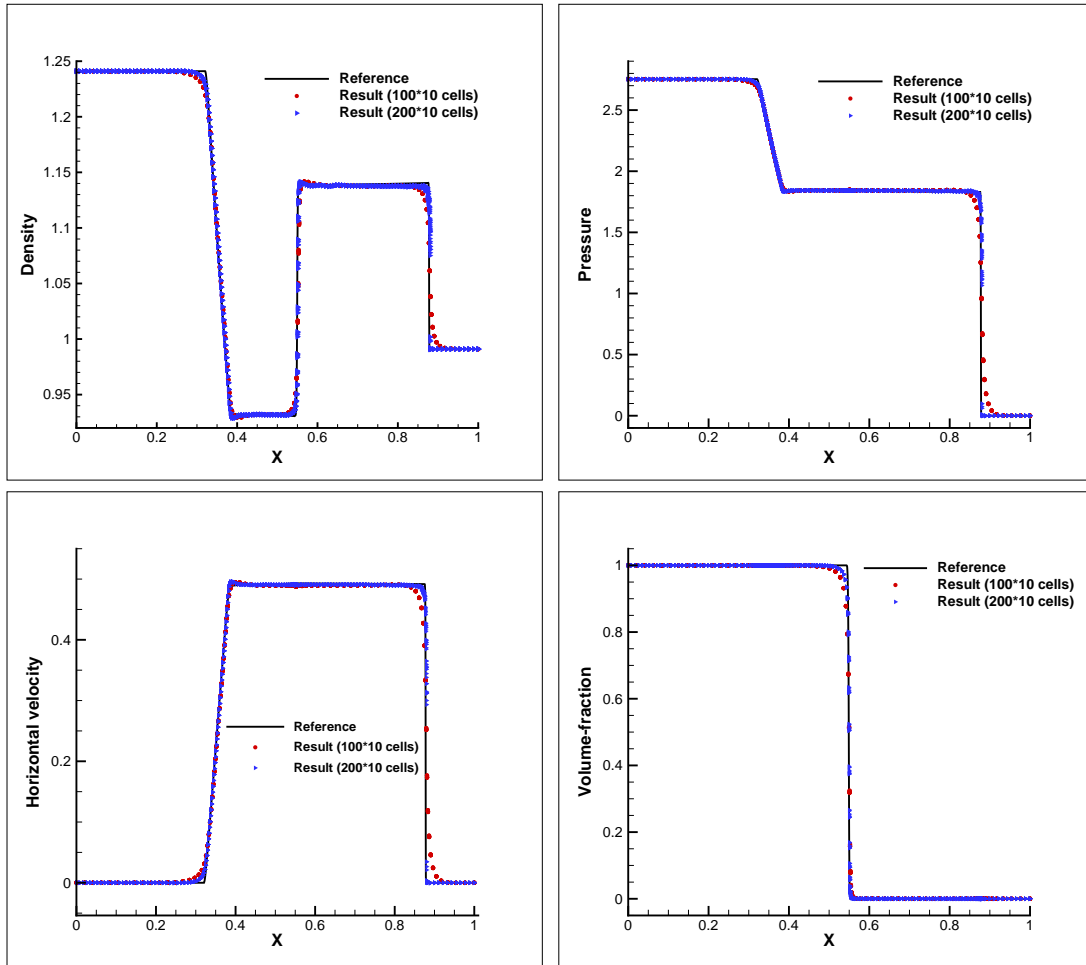


Figure 3: The two-phase gas-liquid Riemann problem at $t=0.1$. Top left: the density; top right: the pressure; bottom left: the horizontal velocity; bottom right: the volume-fraction of gas phase.

interface' located at the dividing line of two regions. The detailed initial values are shown as follows:

$$(\rho, u, v, p, \gamma, \Phi) = \begin{cases} (1.0, 0.0, 0.0, 1.0, 1.4, 1), & \text{left,} \\ (1.5, 0.0, 0.0, 1.0, 1.67, 0), & \text{right.} \end{cases}$$

The upper boundary and the lower boundary are all reflective boundaries, and the left boundary is a piston which moves to the right with a horizontal velocity 1.48. This problem will run to a final time $t = 1.3$. In the code of this case, we set $\alpha_1 = 0$ and $\alpha_2 = 0.03$.

Fig. 5 shows the result consisting of the mesh, the density contours and the volume-fraction contours at $t = 1.3$. It can be seen that though there is a certain numerical dissipation near the material interface because of the characteristic of diffusion interface models, the wave structures are well resolved and the material interface is relatively sharply

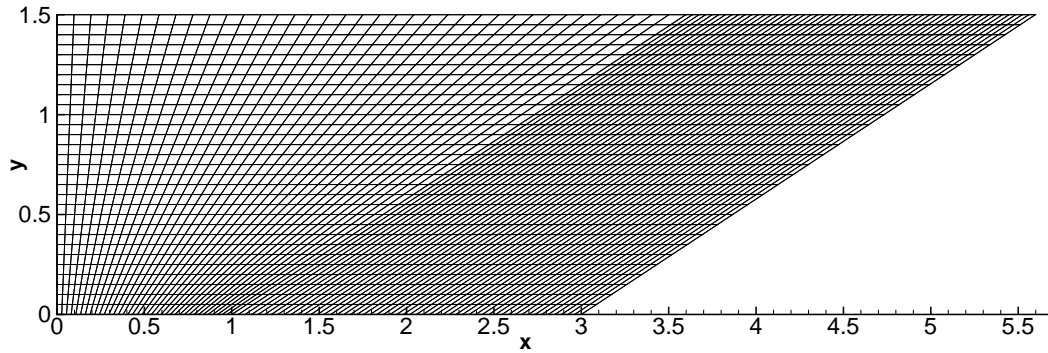


Figure 4: The initial computational domain and the initial mesh of the Dukowicz refraction problem.

captured. Meanwhile, the final mesh keeps good-quality. This case can verify that our scheme keeps good capability of capturing the wave structures and can carry out the simulations of multi-material flows well.

4.4 The triple point problem

The triple point problem [57] is a two-material problem which corresponds to a three states two-dimensional Riemann problem in a rectangular domain. This problem is often used to assess the capability of simulating multi-material flows and the robustness of the numerical scheme because of the significant vorticity, the large shear, and the complex interacting shocks. The computational domain $\Omega = [0,7] \times [0,3]$ is split into three sub-domains $\Omega_1 = [0,1] \times [0,3]$, $\Omega_2 = [1,7] \times [0,1.5]$ and $\Omega_3 = [1,7] \times [1.5,3]$. Ω_1 contains a high-pressure and high-density gas with the initial state: $(\rho_1, p_1, \mathbf{V}_1, \Phi_1) = (1, 1, \mathbf{0}, 1)$. Ω_2 contains a low-pressure and high-density gas with the initial state $(\rho_2, p_2, \mathbf{V}_2, \Phi_2) = (1, 0.1, \mathbf{0}, 0)$. Ω_3 contains a low-pressure, low-density gas whose initial state is $(\rho_3, p_3, \mathbf{V}_3, \Phi_3) = (0.125, 0.1, \mathbf{0}, 1)$. Ω_1 and Ω_3 are filled with the same material characterized by the polytropic index $\gamma_1 = \gamma_3 = 1.5$, whereas Ω_2 is filled with a different material with $\gamma_2 = 1.4$.

This simulation is carried out with 140×60 elements, and the final time is $t = 8$. We set $\alpha_1 = 0$ and $\alpha_2 = 0.2$ in this case. Due to the difference of the acoustic impedance, two shocks in Ω_2 and Ω_3 propagate with different speeds, which creates a strong shear along the initial contact discontinuity located at the interface between Ω_2 and Ω_3 . The shear produces a Kelvin-Helmholtz instability and a vortex structure occurs. Capturing the vortex may be difficult when some methods such as the pure Lagrangian methods are used.

The meshes, the distributions of density and the distributions of volume-fraction at $t = 3.5, 5, 8$ are shown in Fig. 6. As illustrated, our scheme captures the wave structures including the material interface relatively clearly with the help of the adaptive mesh, though there is a certain numerical dissipation near the material interface.

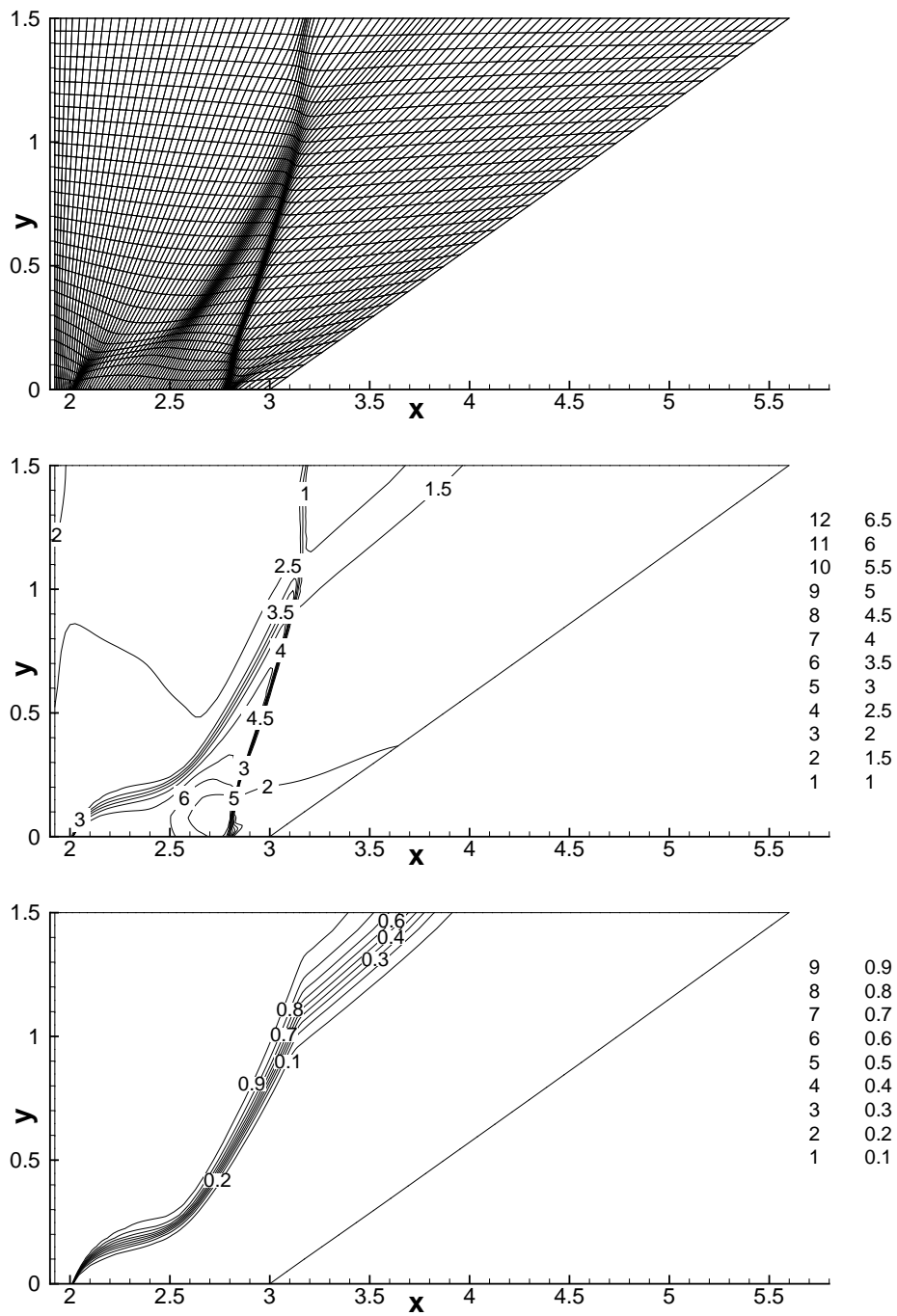


Figure 5: The Dukowicz refraction problem at $t=1.3$. Top: the adaptive mesh; middle: the density contours; bottom: the volume-fraction contours.

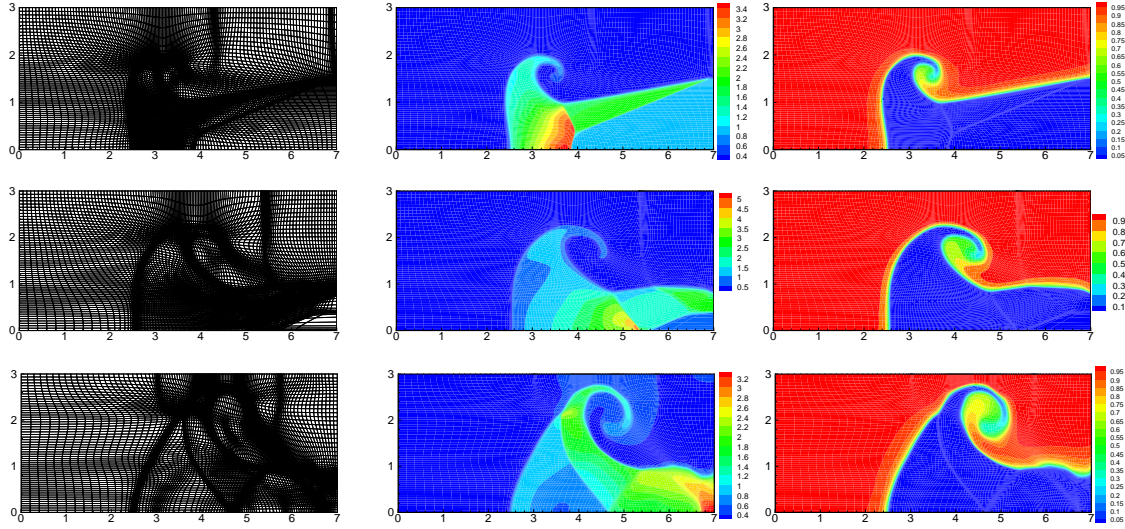


Figure 6: The triple point problem at $t=3.5, 5, 8$ (top to bottom). Left: the adaptive meshes; middle: the distributions of density; right: the distributions of volume-fraction.

4.5 The shock wave and a Helium cylindrical bubble interaction

This case has been extensively studied by many authors, see e.g. [58]. It describes the interaction of a shock wave with a cylindrical Helium bubble surrounded by air at rest. The computational domain is $[0, 325] \times [-44.5, 44.5]$ with the top and the bottom reflective boundaries, the left inflow and the right outflow boundaries. The bubble is assumed to be in both thermal and mechanical equilibrium with the surrounding air. A shock wave with Mach number $M_s = 1.22$ moves to the left. The initial condition is determined by the shock condition with the given shock Mach number. More detailedly, the initial data is set to

$$(\rho, u, v, p, \gamma, \Phi) = \begin{cases} (1, 0, 0, 1, 1.4, 1), & 0 \leq x \leq 225, \quad -44.5 \leq y \leq 44.5, \\ (1.3764, -0.394, 0, 1.5698, 1.4, 1), & 225 < x \leq 325, \quad -44.5 \leq y \leq 44.5, \\ (0.1358, 0, 0, 1, 1.67, 0), & \sqrt{(x-175)^2 + y^2} \leq 25. \end{cases}$$

Here, the initial mesh consists of 240×60 rectangular elements, and we use the artificial parameters $\alpha_1 = 0$ and $\alpha_2 = 0.17$ to control the mesh motion.

The results at $t=75, 120, 150$ which include the adaptive meshes and the density maps are shown in Fig. 7. The shape of bubble is strongly distorted and the results show that the material interfaces are resolved well and accurately. In addition, Fig. 8 shows the comparison between the density map of bubble at $t=150$ obtained by our scheme and the schlieren image of the density of bubble at $t=150$ obtained by a second-order adaptive finite volume method in [59]. It is obvious that the profile of the bubble structure obtained by our scheme is similar to the one in [59] for reference. This case can verify that our

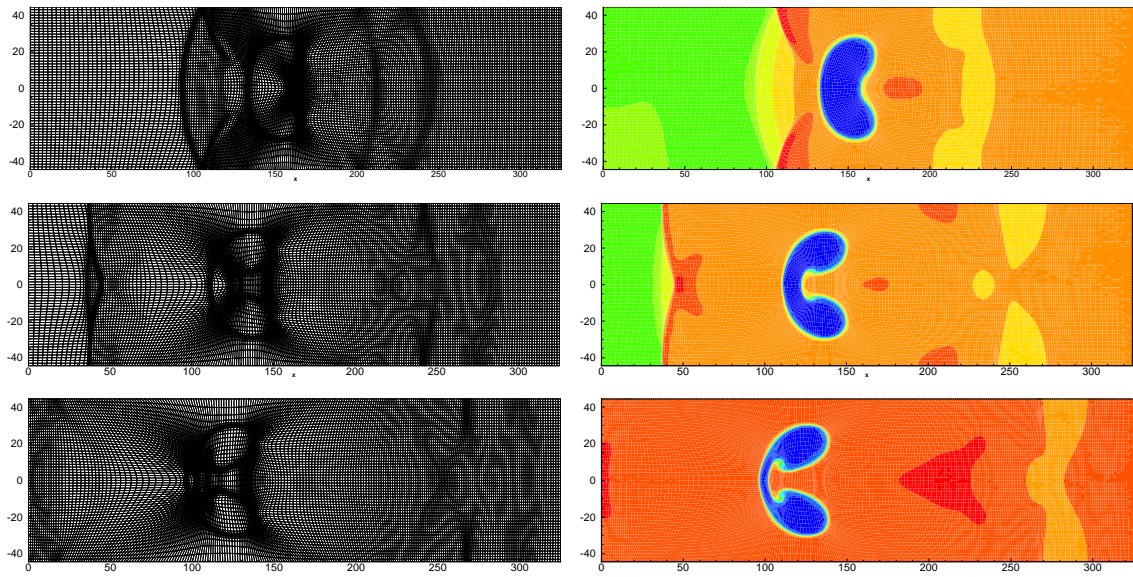


Figure 7: The shock wave and a Helium cylindrical bubble interaction at $t=75,120,150$ (top to bottom). Left: the meshes; right: the density maps.

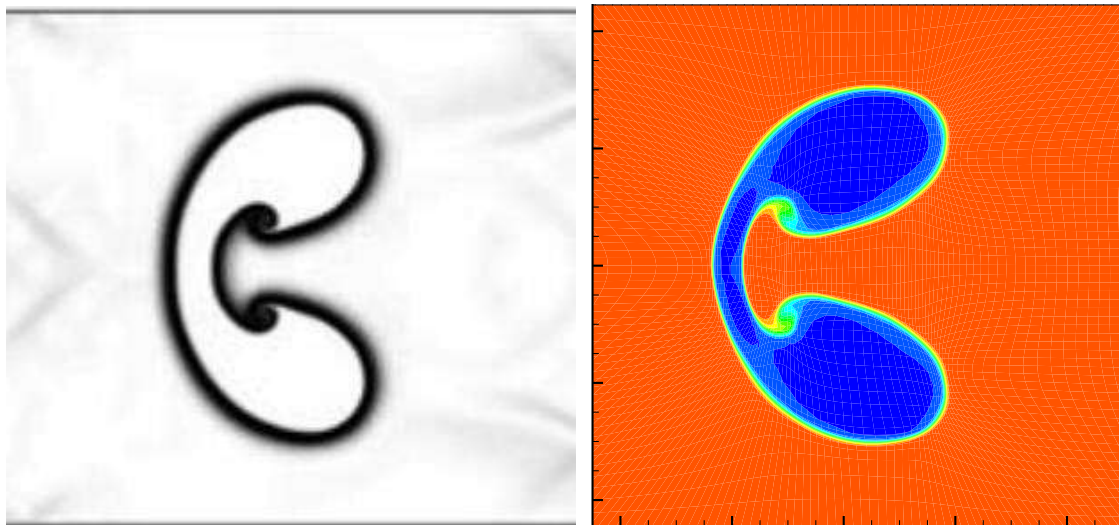


Figure 8: The shock wave and a Helium cylindrical bubble interaction at $t=150$. Left: the schlieren image of the density of bubble in [59]; right: the density map of bubble obtained by our scheme.

scheme has the capability of carrying out the simulations of multi-material flows with large deformations.

4.6 The shock wave and a R22 cylindrical bubble interaction

This case is similar to the above one, but the present gas R22 in the bubble is heavier than air. When these two gases interact with the shock, they will yield different flow patterns around the material interface. The computational domain, the initial rectangular mesh elements, the artificial parameters in the adaptive motion, and the boundary conditions are same as those of the above case. The initial data of this problem is set to

$$(\rho, u, v, p, \gamma, \Phi) = \begin{cases} (1, 0, 0, 1, 1.4, 1), & 0 \leq x \leq 225, \quad -44.5 \leq y \leq 44.5, \\ (1.3764, -0.394, 0, 1.5698, 1.4, 1), & 225 < x \leq 325, \quad -44.5 \leq y \leq 44.5, \\ (3.1538, 0, 0, 1, 1.249, 0), & \sqrt{(x-175)^2 + y^2} \leq 25. \end{cases}$$

The results at $t=60, 100, 150$ which include the adaptive meshes and the density maps are shown in Fig. 9. We can see that the wave structures are captured well and the meshes have good qualities. At the final time $t=150$, the shape of bubble is strongly distorted and the material interface is resolved well and accurately. This case can also verify that our scheme has the capability of carrying out the simulations of multi-material flows with large deformations.

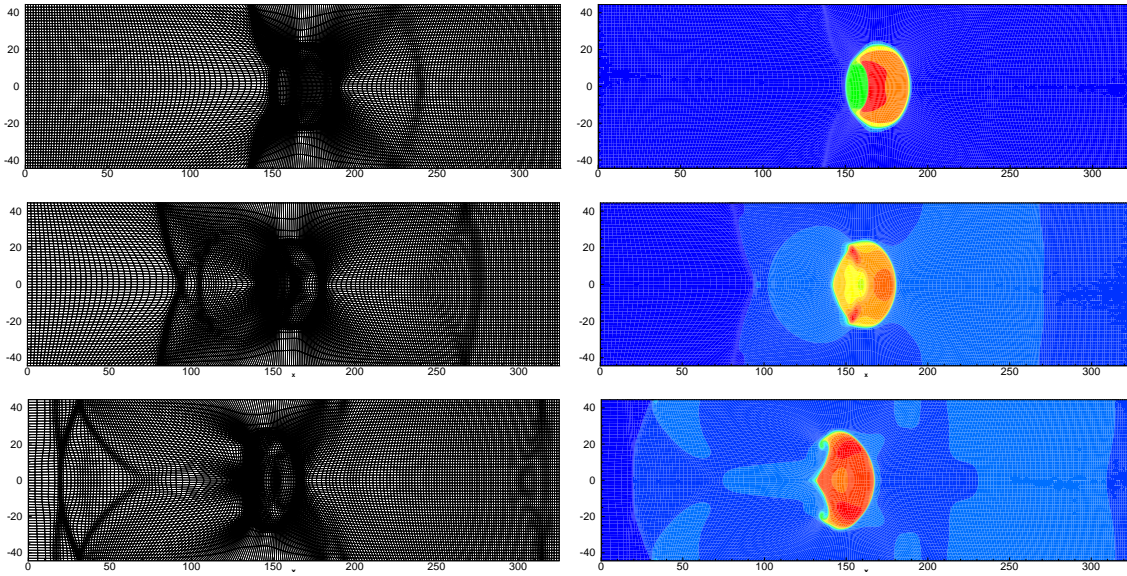


Figure 9: The shock wave and a Helium cylindrical bubble interaction at $t=60, 100, 150$ (top to bottom). Left: the meshes; right: the density maps.

4.7 The 2D underwater explosion problem of the air bubble

In this case, we will study a gas-liquid radially symmetric problem in which an initially at rest circular air bubble is exploded under the water because of the pres-

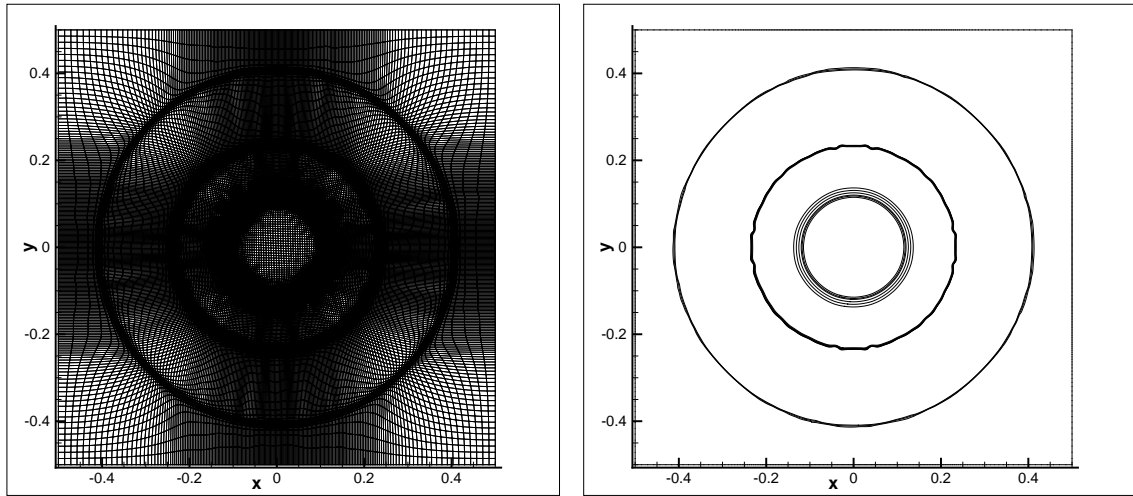


Figure 10: The result of the underwater explosion problem obtained by our ALE-DG scheme with 200×200 adaptive mesh elements. Left: the adaptive mesh; right: the density contours.

sure difference [29]. The breaking of the bubble will result in an outgoing radially shock wave and an incoming rarefaction wave, meanwhile there is a contact discontinuity between these wave structures. We will use the same set of the initial data as in Example 4.2: Inside the bubble with radius $R = 0.2$, the fluid is air with $(\rho_1, u_1, v_1, p_1, \gamma_1, B_1, \Phi_1) = (1.241, 0, 0, 2.753, 1.4, 0, 1)$; while outside the bubble, the fluid is water with $(\rho_2, u_2, v_2, p_2, \gamma_2, B_2, \Phi_2) = (0.991, 0, 0, 3.059 \times 10^{-4}, 5.5, 1.505, 0)$. Under these conditions, the simulation is performed by using our ALE-DG scheme in an initial computational domain $[-0.5, 0.5] \times [-0.5, 0.5]$ with 200×200 mesh elements. In the algorithm of the adaptive mesh motion, we set $\alpha_1 = 0$ and $\alpha_2 = 0.26$.

The density contours and the adaptive mesh at the final time $t = 0.058$ are shown in Fig. 10. As illustrated in Fig. 10, we can see that our scheme quite sharply captures the wave structures duo to the adaptive concentration of mesh nodes. For comparing with the simulation of our ALE-DG scheme on the adaptive mesh, we implement the simulation by our scheme with $\mathbf{V}^g = \mathbf{0}$ and in this situation our scheme evolves into a DG scheme on the fixed uniform mesh (that is, a DG scheme in the Eulerian form). In addition, the density contours obtained by our DG scheme on the fixed uniform meshes with 200×200 elements and 800×800 elements at $t = 0.058$ are given in Fig. 11, respectively. The density contours on the adaptive moving mesh with 200×200 elements are evidently better-resolved than the ones on the fixed mesh with 200×200 elements, and the resolution of density contours on the adaptive mesh with 200×200 elements is similar to the one on the fixed mesh with 800×800 elements. For more clarity, we also show a comparison of the density distribution along the positive half-axis of x -axis obtained by our ALE-DG scheme on the adaptive mesh of 200×200 elements and the one obtained by our DG scheme on the fixed mesh of 200×200 elements in Fig. 12. Finally, we give the com-

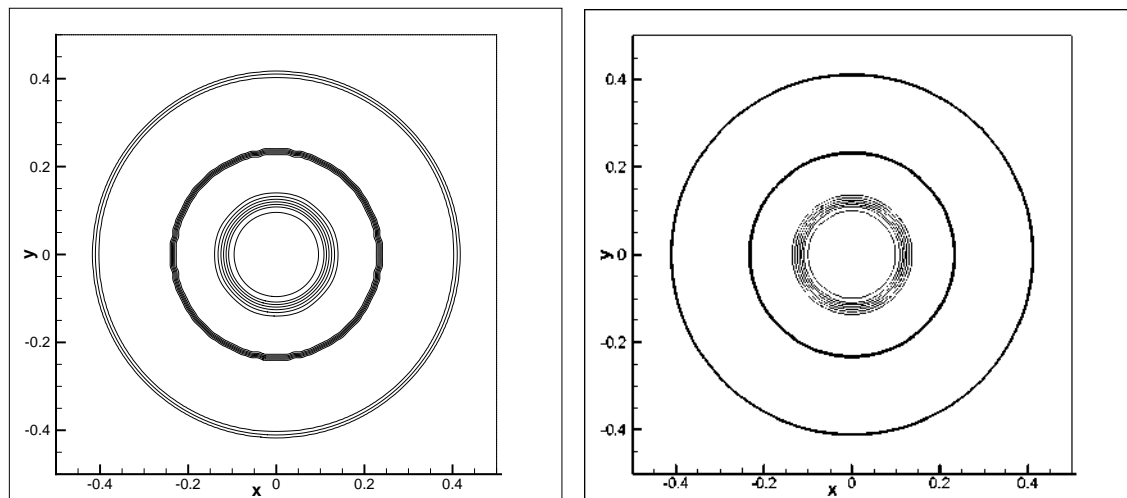


Figure 11: The density contours of the underwater explosion problem obtained by our DG scheme on the fixed meshes. Left: 200×200 elements; right: 800×800 elements.

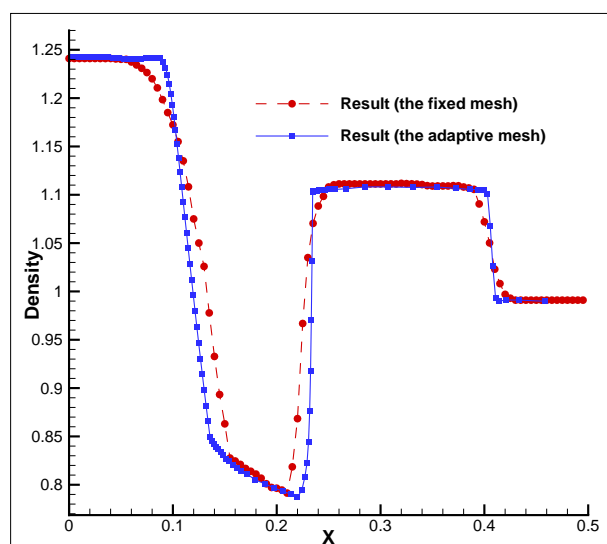


Figure 12: The density distribution along the positive half-axis of x -axis obtained by our ALE-DG scheme on the adaptive mesh with 200×200 elements and the one obtained by our DG scheme on the fixed mesh with 200×200 elements.

parison between the CPU time consumed by the three simulations in Table 3. Under the precondition of keeping other conditions same, compared with the DG schemes using the fixed meshes, our ALE-DG scheme with the adaptive mesh has obvious advantage in the quality of the result with an acceptable computational cost.

Table 3: The comparison between the CPU time consumed by the simulations of DG scheme on the fixed meshes and the one of ALE-DG scheme on the adaptive mesh.

Schemes	CPU time consumed (seconds)
DG scheme with 200×200 fixed mesh elements	25475
DG scheme with 800×800 fixed mesh elements	365842
ALE-DG scheme with 200×200 adaptive mesh elements	74534

5 Conclusions

In this paper, we have proposed a direct ALE-DG scheme for compressible multi-material flows on the adaptive quadrilateral meshes. A conservative equation related to the volume fraction is coupled with the Euler equations to identify the fluid components of the fluid mixture, which makes the system can be applied into the simulations of multi-material flows conveniently. The mesh velocity in the ALE framework is given by the adaptive mesh method [35] which can not only automatically concentrate the mesh nodes near the regions with large gradient values of variables but also help the mesh remain the good quality. Without considering a mesh repair algorithm, the meshes in our simulations have not been too deteriorated, and the adaptive mesh method has greatly improved the resolution of the solution near the regions involving large gradient values and the computational efficiency of the simulations. Our scheme applies to the simulations for two-component flows involving the compressible ideal gases or water medium in two-dimensional geometry. Several examples are presented to demonstrate the accuracy and the good properties of our scheme. Considering the effectiveness and the simplicity of our algorithm, our scheme is competitive when it is compared with some other schemes.

Acknowledgments

This work is supported by National Natural Science Foundation of China (Grant Nos. 12071046, 11571002, 11772067).

References

- [1] Woodward P and Colella P. The numerical simulation of two dimensional fluids with strong shock. *J. Comput. Phys.* 54(1984) 115-173.
- [2] Swartz B K and Wendroff B. AZTEC: A front tracking code based on Godunov's method. *Appl. Numer. Math.* 2 (1986) 385-397.
- [3] Benson D J. Computational methods in Lagrangian and Eulerian hydrocodes. *Comput. Methods Appl. Mech. Eng.* 99 (1992) 235-394.
- [4] Glimm J, Li X and Liu Y, et al. Conservative front tracking with improved accuracy. *SIAM. J. Numer. Anal.* 41 (2003) 1926-1947.

- [5] Shu C and Osher S. Efficient implementation of essentially non-oscillatory shock capturing schemes. *J. Comput. Phys.* 77 (1988) 439-471.
- [6] Shu C and Osher S. Efficient implementation of essentially non-oscillatory shock capturing schemes II. *J. Comput. Phys.* 83 (1989) 32-78.
- [7] Després B and Mazeran C. Lagrangian gas dynamics in two dimensions and Lagrangian systems. *Arch. Rational Mech. Anal.* 178 (2005) 327-372.
- [8] Maire P H, Abgrall R and Breil J, et al. A cell-centered Lagrangian scheme for two-dimensional compressible flow problems. *SIAM J. Sci. Comput.* 29 (2007), 1781-1824
- [9] Dobrev V A, Ellis T E and Kolev T V, et al. Curvilinear finite elements for Lagrangian hydrodynamics. *Int. J. Numer. Meth. Fluids.* 65 (2011) 1295-1310.
- [10] Dobrev V A, Kolev T V and Rieben R N. High-order curvilinear finite element methods for Lagrangian hydrodynamics. *SIAM J. Sci. Comput.* 34 (2012) B606-B641.
- [11] Dobrev V A, Ellis T E, Kolev T V and Rieben R N. High-order curvilinear finite elements for axisymmetric Lagrangian hydrodynamics. *Comput. Fluids.* 83 (2013) 58-69.
- [12] Maire P H, Abgrall R and Breil J, et al. A nominally second-order cell-centered Lagrangian scheme for simulating elastic-plastic flows on two-dimensional unstructured grids. *J. Comput. Phys.* 235 (2013) 626-665.
- [13] Sambasivan S K, Shashkov M J and Burton D E. A finite volume cell-centered Lagrangian hydrodynamics approach for solids in general unstructured grids. *Int. J. Numer. Meth. Fluids.* 72 (2013) 770-810.
- [14] Wu T, Shashkov M and Morgan N, et al. An updated Lagrangian discontinuous Galerkin hydrodynamic method for gas dynamics. *Comput Math. Appl.* 78(2) (2019) 258-273.
- [15] Hirt C, Amsden A and Cook J. An arbitrary Lagrangian Eulerian computing method for all flow speeds. *J. Comput. Phys.* 14 (1974) 227-253.
- [16] Margolin L G. Introduction to an arbitrary Lagrangian-Eulerian computing method for all flow speeds. *J. Comput. Phys.* 135 (1997) 198-202.
- [17] Barlow A J, Maire P H, Rider W J, Rieben R N and Shashkov M J. Arbitrary Lagrangian-Eulerian methods for modeling high-speed compressible multimaterial flows. *J. Comput. Phys.* 322 (2016) 603-665.
- [18] Qing F, Yu X, Jia Z, Qiu M and Zhao X. A high-order cell-centered discontinuous Galerkin multi-material arbitrary Lagrangian-Eulerian method. *Commun. Comput. Phys.* 28 (2020) 1464-1501.
- [19] Xu X, Ni G and Jiang S. A high-order moving mesh kinetic scheme based on WENO reconstruction for compressible flows on unstructured meshes. *J. Sci. Comput.* 57 (2013) 278-299.
- [20] Gaburro E, Boscheri W and Chiochetti S, et al. High order direct arbitrary-Lagrangian-Eulerian schemes on moving Voronoi meshes with topology changes. *J. Comput. Phys.* 407 (2019) 109-167.
- [21] Zhao X, Yu X, Duan M, Qing F and Zou S. An arbitrary Lagrangian-Eulerian RKDG method for compressible Euler equations on unstructured meshes: Single-material flow. *J. Comput. Phys.* 396 (2019) 451-469.
- [22] Wang C, Luo H and Shashkov M. A reconstructed discontinuous Galerkin method for compressible flows in Lagrangian formulation. *Comput. Fluids.* 202 (2020) 104522.
- [23] Wang C and Luo H. A reconstructed discontinuous Galerkin method for compressible flows on moving curved grids. *Adv. Aerodyn.* 3 (2021) 1-28.
- [24] Abgrall R. How to prevent oscillations in multicomponent flow calculations: A quasi conservative approach. *J. Comput. Phys.* 125 (1996) 150-160.
- [25] Abgrall R and Saurel R. Computations of compressible multifluids. *J. Comput. Phys.* 169

- (2001) 594-623.
- [26] Abgrall R and Saurel R. Discrete equations for physical and numerical compressible multi-phase mixtures. *J. Comput. Phys.* 186 (2003) 61-396.
 - [27] Karni S. Multicomponent flow calculations by a consistent primitive algorithm. *J. Comput. Phys.* 112 (1994) 31-43.
 - [28] Karni S. Hybrid multifluid algorithms. *SIAM J. Sci. Comput.* 17 (1996) 1019-1039.
 - [29] Shyue K M. An efficient shock-capturing algorithm for compressible multicomponent problems. *J. Comput. Phys.* 142 (1998) 208-242.
 - [30] Allaire G, Clerc S and Kokh S. A five-equation model for the simulation of interfaces between compressible fluids. *J. Comput. Phys.* 181 (2002) 577-616.
 - [31] Zheng H, Shu C, Chew Y and Qin N. A solution adaptive simulation of compressible multi-fluid flows with general equation of state. *Int. J. Numer. Meth. Fluids.* 67 (2011) 616-637.
 - [32] Winslow A. Numerical solution of the quasi-linear Poisson equation. *J. Comput. Phys.* 1 (1967) 149-172.
 - [33] Miller K and Miller R N. Moving finite element. *SIAM J. Numer. Anal.* 18 (1981) 1019-1032.
 - [34] Cao W, Huang W and Russell R D. An r-adaptive finite element method based upon moving mesh PDEs. *J. Comput. Phys.* 149 (1999) 221-244.
 - [35] Tang H and Tang T. Adaptive mesh methods for one- and two-dimensional hyperbolic conservation laws. *Siam J. Numer. Anal.* 41 (2003) 487-515.
 - [36] Tang H, Tang T and Zhang P. An adaptive mesh redistribution method for nonlinear Hamilton-Jacobi equations in two- and three- dimensions. *J. Comput. Phys.* 188 (2003) 543-572.
 - [37] Duan J and Tang H. Entropy stable adaptive moving mesh schemes for 2D and 3D special relativistic hydrodynamics. *J. Comput. Phys.* 426 (2021) 109949.
 - [38] Duan J and Tang H. High-order accurate entropy stable adaptive moving mesh finite difference schemes for special relativistic (magneto) hydrodynamics. *J. Comput. Phys.* 456 (2022) 111038.
 - [39] Li S, Duan J and Tang H. High-order accurate entropy stable adaptive moving mesh finite difference schemes for (multi-component) compressible Euler equations with the stiffened equation of state. *Comput. Methods Appl. Mech. Engrg.* 399(2022)115311.
 - [40] Han E, Li J and Tang H. Accuracy of the adaptive GRP scheme and the simulation of 2-D Riemann problems for compressible Euler equations. *Commun. Comput. Phys.* 10 (2011) 577-609.
 - [41] Ni G, Jiang S and Xu K. Remapping-free ALE-type kinetic method for flow computations. *J. Comput. Phys.* 228 (2009) 3154-3171.
 - [42] Boscheri W, Dumbser M and Gaburro E. Continuous finite element subgrid basis functions for discontinuous Galerkin schemes on unstructured polygonal Voronoi meshes. *Commun. Comput. Phys.* 32 (2022) 259-298.
 - [43] Zhang F and Liu T. A high-order direct discontinuous Galerkin method for variable density incompressible flows. *Commun. Comput. Phys.* 32 (2022) 850-877.
 - [44] Zhang W, Xing Y, Xia Y and Xu Y. High-order positivity-preserving well-balanced discontinuous Galerkin methods for Euler equations with gravitation on unstructured meshes. *Commun. Comput. Phys.* 31 (2022) 771-815.
 - [45] Xu Y, Chen X, Zhang W and Pan X. An adaptive modal discontinuous Galerkin finite element parallel method using unsplit multi-axial perfectly matched layer for seismic wave modeling. *Commun. Comput. Phys.* 31 (2022) 1083-1113.
 - [46] Liu X, Morgan N R and Burton D E. A high-order Lagrangian discontinuous Galerkin hy-

- drodynamic method for quadratic cells using a subcell mesh stabilization scheme. *J. Comput. Phys.* 386 (2019) 110-157.
- [47] Qing F, Yu X and Jia Z, et al. A cell-centered Lagrangian discontinuous Galerkin method using WENO and HWENO limiter for compressible Euler equations in two dimensions. *Comput. Appl. Math.* 40 (2021) 1-33.
- [48] Farhat C, Geuzaine P and Grandmont C. The discrete geometric conservation law and the nonlinear stability of ALE schemes for the solution of flow problems on moving grids. *J. Comput. Phys.* 174 (2001) 669-694.
- [49] Cockburn B and Shu C. The Runge-Kutta discontinuous Galerkin method for conservation laws II: General framework. *Math. Comp.* 52 (1989) 411-435.
- [50] Cockburn B and Shu C. The Runge-Kutta discontinuous Galerkin method for conservation laws V: Multidimensional systems. *J. Comput. Phys.* 141 (1998) 199-224.
- [51] Jia Z and Zhang S. A new high-order discontinuous Galerkin spectral finite element method for Lagrangian gas dynamics in two dimensions. *J. Comput. Phys.* 230 (2011) 2496-522.
- [52] Vilar F. Cell-centered discontinuous Galerkin discretization for two-dimensional Lagrangian hydrodynamics. *Comput. Fluids.* 64 (2012) 64-73.
- [53] Maire P H and Breil J. A second-order cell-centered Lagrangian scheme for two-dimensional compressible flow problems. *Int. J. Numer. Meth. Fl.* 56 (2008) 1417-1423.
- [54] LeVeque R J and Shyue K M. One-dimensional front tracking based on high resolution wave propagation methods. *SIAM J. Sci. Comput.* 16 (1995) 348-377.
- [55] Dukowicz J K and Meltz B. Vorticity errors in multidimensional Lagrangian codes. *J. Comput. Phys.* 99 (1992) 115-134.
- [56] Cheng J and Shu C. A high order ENO conservative Lagrangian type scheme for the compressible Euler equations. *J. Comput. Phys.* 227 (2007) 1567-1596.
- [57] Loubère R, Maire P H and Shashkov M, et al. ReALE: A reconnection-based arbitrary-Lagrangian-Eulerian method. *J. Comput. Phys.* 229 (2010) 4724-4761.
- [58] Quirk J J and Karni S. On the dynamics of a shock-bubble interaction. *J. Fluid Mech.* 318 (1996) 129-163.
- [59] Chen G, Tang H and Zhang P. Second-order accurate Godunov scheme for multicomponent flows on moving triangular meshes. *J. Comput. Phys.* 34 (2008) 64-86.